

# Spin dynamics of moving bodies in rotating black hole spacetimes

Balázs Mikóczy<sup>1,†</sup> and Zoltán Keresztes<sup>2,‡</sup>

<sup>1</sup> *Research Institute for Particle and Nuclear Physics,*

*Wigner RCP H-1525 Budapest 114, P.O. Box 49, Hungary*

<sup>2</sup> *Department of Theoretical Physics, University of Szeged, Tisza Lajos krt. 84-86, Szeged 6720, Hungary*

<sup>†</sup>*E-mail: mikoczy.balazs@wigner.hu* <sup>‡</sup>*E-mail: zkeresztes@titan.physx.u-szeged.hu*

The dynamics of spinning test bodies, moving in rotating black hole (Kerr, Bardeen-like and Hayward-like) spacetimes, are investigated. In Kerr spacetime, all the spherical, zoom-whirl and unbound orbits are considered numerically. Along spherical orbits and for high spin, an amplitude modulation is found in the harmonic evolution of the spin precessional angular velocity, caused by the spin-curvature coupling. Along the discussed zoom-whirl and unbound orbits, the test body approaches the center so much that it passes through the ergosphere. Near and inside the ergosphere, the variation of the spin direction can be very rapid. The effects of the spin-curvature coupling is also investigated. The initial values are chosen such a way, that the body and its spin move in the equatorial plane of the coordinate space and of the comoving frame, respectively. Hence, a clear effect of the spin-curvature coupling is observed as the orbit and the spin vector leave the equatorial plane. Additional effects in the spin precessional angular velocity and in the evolution of the Boyer-Lindquist coordinate components of the spin vector is also considered. Finally, in case of different regular black holes, the spin-curvature coupling influences differently the orbit and the spin evolutions.

Keywords: black hole physics, spinning test particles, Mathisson-Papapetrou-Dixon equations, Kerr spacetime

## I. INTRODUCTION

Both the orbital and the spin dynamics of compact binary systems have a renewed interest. All observed gravitational waves originated from compact binary systems composed of black holes or neutron stars ([1–8]). In two cases the spin of the merging black holes was identified with high significance [2, 8, 9]. In addition, in a binary system the dominant supermassive black hole spin precession was identified from VLBI radio data spanning over 18 years [10].

In the post-Newtonian (PN) approximation the lowest order spin contributions to the dynamics come from the spin-orbit, spin-spin and quadrupole-monopole interactions [11–14]. The spin effects on the orbit lead to set up generalized Kepler equations [15–18]. The analytical description of the secular spin dynamics for black holes is given in Refs. [19] and [20]. Based on the PN description several interesting spin related behaviours were identified in compact binary systems, like transitional precession [21], equilibrium configurations [22], spin-flip [23], spin flip-flop [24] and wide precession [25].

The Mathisson-Papapetrou-Dixon (MPD) equations [26–30] describe the dynamics of binaries with significantly different masses more accurately than the PN approximation in the strong gravitational field regime, where the PN parameter is not small. The black hole binary systems with small mass ratio are among the most promising sources for gravitational waves in the frequency sensitivity range of the planned LISA - Laser Interferometer Space Antenna [31, 32]. In addition, near the central supermassive black holes in the galaxies many stellar black holes are expected to exist [33–35].

The MPD equations are not closed, a spin supplemen-

tary condition<sup>1</sup> (SSC) is necessary to choose [28, 37–44], which defines the point at which the four-momentum and the spin are evaluated. The Hamiltonian formulations in different SSCs are discussed in Refs. [45–49]. A non-spinning body follows a geodesic trajectory, while a spinning one does not [50, 51]. Spinning bodies governed by the MPD equations were already studied on Kerr background. Circular orbits in the equatorial plane can be unstable not only in the radial direction but also in the perpendicular direction to the equatorial plane due to the spin [52]. The spin-curvature effect strengthens with spin and with non-homogeneity of the background field [51]. The MPD equations admit many chaotic solutions, however, these do not occur in the case of extreme mass ratio binary black hole systems [53–56]. Analytic studies on the deviation of the orbits from geodesics due to the presence of a small spin are presented in Refs. [57–59]. Highly relativistic circular orbits in the equatorial plane occur in much wider space region for a spinning body than for a non-spinning one [60]. Spin-flip-effects may occur when the magnetic type components of quadrupole tensor are non-negligible [61]. Corrections due to the electric type components of quadrupole tensor to the location of innermost stable circular orbit in the equatorial plane and to the associated motion's frequency were determined in Ref. [62]. An exact expression for the periastron shift of a spinning test body moving in the equatorial plane is derived in Ref. [63]. The influences of the affine parameter choice on the constants of motion in different SSC

<sup>1</sup> Both the PN dynamics with spin-orbit coupling and the gravitational multipole moments depend on the SSC [13, 36].

were also considered [64]. Frequency domain analysis of motion and spin precession was presented in Ref. [65]. The evolution of spinning test particles were investigated in the  $\gamma$  space-time [66], in non-asymptotically flat spacetimes [67], and in wormholes [68].

Considering geodesic trajectories, the periastron advance can become such significant in the strong gravitational field regime that the test particle follows a zoom-whirl orbit [69–71]. For non-spinning particles, the topology of these orbits was encoded by a rational number [72, 73]. Numerical relativity confirmed the existence of zoom-whirl orbits [74–79], and they also occur in the 3 PN dynamics with spin-orbit interaction [80, 81]. Here we will present zoom-whirl orbits occurring in the MPD dynamics for the first time. In addition, these orbits pass over the ergosphere where the PN approximation fails.<sup>2</sup>

Hyperbolic orbits of spinning bodies were analytically studied in both the PN [82] and the MPD [83] dynamics. Analytic computations in Ref. [83] were carried out for small spin magnitudes, when the spin is parallel to the central black hole rotation axis and the body moves in the equatorial plane. In this configuration both the spin magnitude and direction are conserved, but they have non-negligible influences on the orbit. In our numerical consideration the spin is not parallel to the black hole rotation axis. As a consequence, the body's orbit is not confined to the equatorial plane and the spin direction evolves. In addition, the closest approach distance is inside the ergosphere where the PN approximation cannot be used.

Our investigations are not only applied in the Kerr spacetime but also in regular black hole backgrounds. The first spacetime containing a nonrotating regular black hole was suggested by Bardeen [84]. This metric was interpreted as the spacetime surrounding a magnetic monopole occurring in a nonlinear electrodynamics [85]. Another nonrotating regular black hole was introduced by Hayward [86] having similar interpretation [87]. The spacetime family containing the Bardeen and Hayward cases was generalized for rotating black holes [88] which we will use here<sup>3</sup>.

In this paper, we investigate the orbit and spin evolutions of bodies moving in Kerr, Bardeen-like and Hayward-like spacetimes and governed by the MPD equations with Frenkel–Mathisson–Pirani (FMP) and Tulczyjew–Dixon (TD) SSCs. When the covariant derivatives of the spin tensor and the four-momentum along the integral curve of the centroid determined by the

SSC are small, this system reduces to a geodesic equation with parallel transported spin discussed in Ref. [92]. In this sense the present article can be considered as the generalization of Ref. [92] with non-negligible spin-curvature corrections causing that the centroid orbit is non-geodesic and the spin is not parallel transported. As Bini, Geralico and Jantzen pointed out that the spin dynamics can be described suitably in the comoving Cartesian-like frame obtained by boosting the Cartesian-like frame associated to the family of static observers (SOs). This is because SOs do not move with respect to the distant stars. Hence, the Cartesian-like axes locked to SOs define good reference directions to which the variation of the spin vector can be compared. Here, we derive the spin evolution equation in the comoving Cartesian-like frame based on the MPD system. However, SO does not exist inside the ergosphere of the rotating black hole, and thus its frame cannot be used for description of the dynamics when the spinning body passes over this region. Therefore, the spin dynamics in a Cartesian-like frame obtained by an instantaneous Lorentz-boost from the frame associated to the zero angular momentum observer (ZAMO) is also presented, which can be used inside the ergosphere. The boosted SO and ZAMO frames relate to each other by a spatial rotation outside the ergosphere. The rotation angle between these boosted frames is insignificant far from the rotating black hole.

In Section II, the MPD equations, the spin supplementary conditions, the rotating (Kerr, Bardeen-like and Hayward-like) black hole spacetimes and the frames associated with the families of SOs and ZAMOs are introduced. In Section III the representations of spin evolution are given. For this purpose, we introduce two frames by instantaneous Lorentz boosts of SO and ZAMO frames, which comoves with an observer having an arbitrary four velocity  $U$ . The relation between the boosted frames is discussed (additional expressions are given in Appendix VII). We use the TD SSC, and  $U$  means either the centroid or the zero 3-momentum observer four velocity. The spin evolution equation is derived in these  $U$ -frames. First, the spin precession is described with respect to the boosted spherical coordinate triad associated with either the SOs or ZAMOs. Then, we introduce Cartesian-like triads in the rest spaces of SOs and ZAMOs. The spin precession with respect to the corresponding boosted Cartesian-like frames is also derived. The relations between the spin angular velocities in the boosted SO and ZAMO frames are discussed. In Section IV, we apply the derived spin equations for numeric investigations when the body moves along spherical-like, zoom-whirl and unbound orbits. In Subsection IV A the background is the Kerr spacetime, while in Subsection IV B, it is one of the rotating regular black hole spacetimes. In Appendix VIII, the avoidance of paradoxical behaviour of the MPD equations is checked. Finally, Section V contains the conclusions.

We use the signature  $-+++$ , and units where  $c = G = 1$ , with speed of light  $c$  and gravitational constant

<sup>2</sup> At the ergosphere the value of the PN expansion parameter is typically about  $1/2$ .

<sup>3</sup> There are discussions (see Refs. [89–91]) on that the rotating regular black hole spacetimes given in Ref. [88] are not exact solutions of the field equations. However the spacetime family given analytically differs only perturbatively from the exact solution [91], therefore it is suitable for consideration of spinning bodies evolutions.

$G$ . The bold small Greek indices with or without prime take values 1, 2 and 3, while the bold capital and the small Latin indices 0, 1, 2 and 3. In addition, the following small bold Latin indices  $\mathbf{i}, \mathbf{j}, \mathbf{k}$  and  $\mathbf{i}', \mathbf{k}'$  take values from  $\{\mathbf{x}, \mathbf{y}, \mathbf{z}\}$ . Finally, the bold indices are frame indices, while the non-bold indices are spacetime coordinate indices.

## II. EQUATIONS OF MOTION FOR SPINNING BODIES IN ROTATING BLACK HOLE SPACETIMES

### A. MPD equations and SSC

In the pole-dipole approximation, the motion of an extended spinning body in curved spacetime is governed by the MPD equations [26–30] which read as

$$\frac{Dp^a}{d\tau} \equiv u^c \nabla_c p^a = F^a, \quad (1)$$

$$\frac{DS^{ab}}{d\tau} \equiv u^c \nabla_c S^{ab} = p^a u^b - u^a p^b, \quad (2)$$

with

$$F^a = -\frac{1}{2} R^a_{bcd} u^b S^{cd}. \quad (3)$$

Here  $\nabla_c$  is the covariant derivative,  $p^a$  and  $S^{ab}$  are the four-momentum and the spin tensor of the moving body, respectively, and  $R^a_{bcd}$  is the Riemann tensor. Finally,  $u^a = dx^a/d\tau$  is the four-velocity of the representative point for the extended body at spacetime coordinate  $x^a(\tau)$  with an affine parameter  $\tau$ . Note that higher multipoles of the body should occur in the MDP equations when they are nonvanishing. Here they are taken to be zero.

Choosing the affine parameter  $\tau$  as the proper time [48, 93]  $u^a u_a = -1^4$ , Equation (2) can be written as

$$p^a = m u^a - u_b \frac{DS^{ab}}{d\tau}, \quad (4)$$

where  $m = -u_a p^a$  is the mass in the rest frame of the observer moving with velocity  $u^a$ . Equation (4) shows that the momentum  $p^a$  and the kinematic four velocity  $u^a$  are not proportional to each other for a spinning body in general.

We note that if the covariant derivatives of the spin tensor and the four-momentum along the integral curve of  $u^a$  are small, i.e. the right hand sides of Equations (1) and (2) are negligible,  $p^a$  becomes proportional to  $u^a$

which satisfies the geodesic equation because  $m$  is a constant. Then introducing a spin four-vector perpendicular to  $u^a$  (see Equation (2.5) of Ref. [94]), it will be parallel transported along the trajectory. The geodesic equations with parallel transported spin vector was investigated in Ref. [92].

In general, in order to close the MPD equations an SSC is necessary to choose, which defines the representative point of the extended body referred as the center of mass or the centroid. There are some proposed SSC, namely the Frenkel-Mathisson-Pirani [26, 37, 38], the Newton-Wigner-Pryce [40, 41], the Corinaldesi-Papapetrou [27, 39], and the Tulczyjew-Dixon [28, 42]. We will apply the Tulczyjew-Dixon SSC imposing that

$$p_a S^{ab} = 0. \quad (5)$$

This SSC yields two constants of motion, the spin magnitude  $S^2 = S_{ab} S^{ab}/2$  and the dynamical mass  $M = \sqrt{-p^a p_a}$  (see Ref. [51]). In addition, the TD SSC together with the MPD equations results in the following velocity-momentum relation [51, 95, 96]:

$$u^b = \frac{m}{M^2} \left( p^b + \frac{4S^2}{\eta} v^b \right), \quad (6)$$

with

$$v^b = \frac{S^{ba} R_{aecd} p^e S^{cd}}{2S^2}, \quad (7)$$

and

$$\eta = 4M^2 + 2\alpha_R S^2, \quad (8)$$

where  $\alpha_R = R_{aecd} S^{ae} S^{cd}/2S^2$ . Since  $p^b$  and  $u^b$  are not parallels,  $u^b$  may become spacelike from timelike along an integral curve. Where the causal character of a curve is changed, it is known as superluminal bound and has been discussed in different cases (e.g. Refs.: [51, 66–68]). The superluminal motion has no physical meaning, and the timelike condition for  $u^b$  yields a bound for the spin magnitude as

$$S^2 < \frac{2M^3}{2v - \alpha_R M}, \quad (9)$$

where  $v = \sqrt{v_a v^a}$ <sup>5</sup>. When the spin magnitude obeys this constraint, the proper time parametrization has sense and the normalization  $u^b u_b = -1$  gives a relation  $m^2 = m^2(p^a, S^{bc})$  as

$$m^2 = \frac{M^4}{\left( M^2 - \frac{16S^4}{\eta^2} v^2 \right)}. \quad (10)$$

<sup>4</sup> Below we derive a condition for the spin magnitude in TD SSC when the proper time parametrization has a sense.

<sup>5</sup> Note that  $v$  and  $\alpha_R$  do not carry information on the spin magnitude since  $S^{ab}/\sqrt{2}S$  has unit norm.

Since the relation (6) can be inverted [97], both initial data sets  $\{x^a, p^a, S^{ab}\}|_{\tau_{in}}$  and  $\{x^a, m, u^a, S^{ab}\}|_{\tau_{in}}$  provide a unique solution of the MPD equations with TD SSC.

The spin vector being perpendicular to  $p^a$  is introduced as

$$S^a = -\frac{1}{2M}\eta^{abcd}p_b S_{cd}. \quad (11)$$

Since

$$S_a S^{ab} = 0 = S_a p^a = 0, \quad (12)$$

the contraction of Equation (6) with  $S_b$  results in  $S_b u^b = 0$ . Finally, the covariant derivative of  $S^a$  along the worldline of the centroid is

$$\frac{DS^a}{d\tau} = \frac{S^b F_b}{M^2} p^a. \quad (13)$$

If  $F^a$  is negligible,  $S^a$  is parallel transported along the worldline of the centroid, and the centroid moves along a geodesic curve. The latter can be shown from the MPD equations together with (4) and (13).

Finally, we mention that the MPD equations are valid only for test particles whose backreaction to the background spacetime curvature are negligible. Hence, when the spinning body is moving in a spacetime around a black hole with a mass parameter  $\mu$ , the dimensionless spin magnitude  $S/M\mu$  must be small [53, 98]. This is consistent with the constraint (9), which becomes for the dimensionless spin magnitude as

$$\left(\frac{S}{M\mu}\right)^2 < \frac{2}{2v - \alpha_R M} \frac{M}{\mu}, \quad (14)$$

where the mass ratio  $M/\mu$  gives a small factor.

## B. Rotating black hole spacetimes

The line element squared describing the considered rotating black hole spacetimes in Boyer-Lindquist coordinates reads as [88, 99]

$$ds^2 = -\frac{\Delta - a^2 \sin^2 \theta}{\Sigma} dt^2 - \frac{2a\mathcal{B} \sin^2 \theta}{\Sigma} dt d\phi + \frac{\Sigma}{\Delta} dr^2 + \Sigma d\theta^2 + \frac{\mathcal{A}}{\Sigma} \sin^2 \theta d\phi^2, \quad (15)$$

with

$$\begin{aligned} \Sigma &= r^2 + a^2 \cos^2 \theta, \\ \Delta &= r^2 + a^2 - 2[\mu + \alpha(r)]r, \\ \mathcal{B} &= r^2 + a^2 - \Delta, \\ \mathcal{A} &= (r^2 + a^2)^2 - \Delta a^2 \sin^2 \theta. \end{aligned} \quad (16)$$

In the Kerr spacetime  $\alpha(r)$  vanishes and  $\mu$  and  $a$  denote the mass and rotation parameters, respectively. The

function  $\alpha(r)$  occurs when a non-linear electromagnetic field is present. It is given by

$$\alpha(r) = \frac{\mu_{em} r^\gamma}{(r^\nu + q_m^\nu)^{\gamma/\nu}}, \quad (17)$$

where  $\mu_{em} = q_m^3/\sigma$  is the electromagnetically induced ADM mass. Here  $\sigma$  controls the strength of nonlinear electrodynamic field and carries the dimension of length squared,  $q_m$  is related to the magnetic charge (see Ref. [87]), and the powers are ( $\gamma = 3, \nu = 2$ ) for the Bardeen-like and ( $\gamma = 3, \nu = 3$ ) for the Hayward-like spacetimes.

The stationary limit surfaces and the event horizon (if they exist) are determined by the solutions of equations  $g_{tt} = \Delta - a^2 \sin^2 \theta = 0$  and  $g^{rr} = \Delta = 0$ , respectively. The structure of the spacetime depends on the number of real, positive solutions of these equations. For the Kerr spacetime  $\mu_{em} = 0$ , then there are two stationary limit surfaces and event horizons for  $a/\mu < 1$ . The region which is located outside the outer event horizon but inside the outer stationary limit surface is called ergosphere. The spacetime is free from the singularity for  $\mu = 0$  and  $\gamma \geq 3$ . The first and the second panels of Figure 3 in Ref. [88] indicate the regions in the parameter space of  $a$  and  $q = q_m/\mu_{em}$  for the Bardeen and the Hayward subcases, respectively, where the above line element squared describes a regular black hole.

In the spacetimes having symmetries, constants of motion associated to each Killing vector  $\xi^a$  (which obeys the Killing equation  $\nabla_{(a}\xi_{b)} = 0$ ) emerge [29]. Since the rotating black hole spacetimes have a timelike  $\partial_t$  and a spatial  $\partial_\phi$  Killing vectors due to the staticity and axial symmetry, there are two constants of motion [53]:

$$\begin{aligned} E &= -p_t - \frac{1}{2} S^{ab} \partial_a g_{bt}, \\ J_z &= p_\phi + \frac{1}{2} S^{ab} \partial_a g_{b\phi}. \end{aligned} \quad (18)$$

At spatial infinity  $E$  means the energy of the spinning body and  $J_z$  is the projection of the total momentum to the symmetry axis. These constants are used for checking the numerical accuracy.

### 1. Static and zero angular momentum observers

The worldlines of static observers are the integral curves of the Killing vector field  $\partial_t$ . This family of observers exists outside the ergosphere, where their frame is given by

$$\begin{aligned} e_0 &= u_{(SO)} = \frac{1}{\sqrt{-g_{tt}}} \partial_t, \quad e_1 = \sqrt{\frac{\Delta}{\Sigma}} \partial_r, \quad e_2 = \frac{\partial_\theta}{\sqrt{\Sigma}}, \\ e_3 &= -\frac{1}{\sqrt{\Delta}} \left( \frac{a\mathcal{B} \sin \theta}{\Sigma \sqrt{-g_{tt}}} \partial_t - \frac{\sqrt{-g_{tt}}}{\sin \theta} \partial_\phi \right). \end{aligned} \quad (19)$$

The dual basis is obtained as  $e_a^{\mathbf{A}} = g_{ab} \eta^{\mathbf{AB}} e_B^b$ , where  $\eta^{\mathbf{AB}} = \text{diag}(-1, 1, 1, 1)$ .

The orbit of a zero angular momentum observer is orthogonal to the  $t = \text{const.}$  hypersurfaces [100, 101]. The four velocity along this orbit is

$$u_{(ZAMO)} = \sqrt{\frac{\mathcal{A}}{\Sigma \Delta}} \left( \partial_t + \frac{a\mathcal{B}}{\mathcal{A}} \partial_\phi \right), \quad (20)$$

which corresponds to the 1-form:  $-dt/\sqrt{-g^{tt}}$ . In contrast to the SOs, this family of observers also exists inside the ergosphere but outside the outer event horizon. The frame of the ZAMOs is given by

$$\begin{aligned} f_0 &= u_{(ZAMO)}, \quad f_1 = \sqrt{\frac{\Delta}{\Sigma}} \partial_r, \\ f_2 &= \frac{\partial_\theta}{\sqrt{\Sigma}}, \quad f_3 = \sqrt{\frac{\Sigma}{\mathcal{A}}} \frac{\partial_\phi}{\sin \theta}, \end{aligned} \quad (21)$$

with dual basis:  $f_a^A = g_{ab} \eta^{AB} f_B^b$ .

### III. REPRESENTATIONS OF SPIN EVOLUTION

The spin vector (11) will be considered in both comoving and zero 3-momentum frames. The definitions of comoving and zero 3-momentum observers will be introduced in the next subsection. Then the spin evolution equations will be derived using the boosted spatial spherical and Cartesian-like triads.

#### A. Comoving and zero 3-momentum frames

In the TD SSC, the center of mass is unique and measured in the zero 3-momentum frame with four velocity  $p^a/M$ . On the other hand the four velocity of the centroid is  $u^a$ . The comoving indicative will refer to that observer which moves along the centroid worldline. The spin dynamics will be described in both the zero 3-momentum and the comoving observer's frames. The velocity of the chosen observer will be denoted by  $U$ . The comoving and zero 3-momentum observers' frames will be set up from the frames of the static and the zero angular momentum observers by an instantaneous Lorentz-boost knowing  $U$  numerically.

The comoving and zero 3-momentum frames (hereafter unanimously referred as  $U$ -frame) obtained from the SO frame are given by

$$E_0(e, U) \equiv U = \Gamma_{(S)} (e_0 + \mathbf{v}_{(S)}),$$

$$E_\alpha(e, U) = e_\alpha + \frac{U \cdot e_\alpha}{1 + \Gamma_{(S)}} (U + u_{(SO)}). \quad (22)$$

Here  $\alpha = \{1, 2, 3\}$ ,  $\mathbf{v}_{(S)} = \Gamma_{(S)}^{-1} U - u_{(SO)}$  is the relative spatial velocity of either the comoving or the zero 3-momentum observer with respect to the SO frame,

which is perpendicular to  $e_0$ , and the Lorentz factor is  $\Gamma_{(S)} = -U \cdot u_{(SO)}$ . The dot denotes the inner product with respect to the metric  $g_{ab}$ . The inverse transformation is given by

$$e_0 = \Gamma_{(S)} (E_0(e, U) + \mathbf{w}_{(S)}),$$

$$e_\alpha = E_\alpha(e, U) + \frac{u_{(SO)} \cdot E_\alpha(e, U)}{1 + \Gamma_{(S)}} (U + u_{(SO)}), \quad (23)$$

where

$$\mathbf{w}_{(S)} = w_{(S)}^\alpha E_\alpha(e, U) = \Gamma_{(S)}^{-1} u_{(SO)} - U, \quad (24)$$

is the relative spatial velocity of the static observer with respect to the  $U$ -frame.

The corresponding Lorentz-boost from the ZAMO frame reads as

$$E_0(f, U) \equiv U = \Gamma_{(Z)} (f_0 + \mathbf{v}_{(Z)}),$$

$$E_\alpha(f, U) = f_\alpha + \frac{U \cdot f_\alpha}{1 + \Gamma_{(Z)}} (U + u_{(ZAMO)}), \quad (25)$$

with relative spatial velocity  $\mathbf{v}_{(Z)} = \Gamma_{(Z)}^{-1} U - u_{(ZAMO)}$  of the  $U$ -frame with respect to the ZAMO frame, and Lorentz factor:  $\Gamma_{(Z)} = -U \cdot u_{(ZAMO)}$ . The inverse boost transformation is given by

$$f_0 = \Gamma_{(Z)} (E_0(f, U) + \mathbf{w}_{(Z)}),$$

$$f_\alpha = E_\alpha(f, U) + \frac{u_{(ZAMO)} \cdot E_\alpha(f, U)}{1 + \Gamma_{(Z)}} (U + u_{(ZAMO)}), \quad (26)$$

where

$$\mathbf{w}_{(Z)} = w_{(Z)}^\alpha E_\alpha(f, U) = \Gamma_{(Z)}^{-1} u_{(ZAMO)} - U, \quad (27)$$

is the relative spatial velocity of the ZAMO with respect to either the comoving or the zero 3-momentum frame.

Since  $E_0(e, U) = U = E_0(f, U)$ , the transformation between the frames  $E_A(e, U)$  and  $E_A(f, U)$  is a rotation in the rest space of either the comoving or the zero 3-momentum observer. The rotation axis has the following non-zero components in both the  $E_A(e, U)$  and the  $E_A(f, U)$  frames:

$$\begin{aligned} n^1 &= -\frac{w_{(Z)}^2}{\sqrt{(w_{(Z)}^1)^2 + (w_{(Z)}^2)^2}} \\ &= -\frac{w_{(S)}^2}{\sqrt{(w_{(S)}^1)^2 + (w_{(S)}^2)^2}}, \end{aligned} \quad (28)$$

and

$$\begin{aligned} n^2 &= \frac{w_{(Z)}^1}{\sqrt{(w_{(Z)}^1)^2 + (w_{(Z)}^2)^2}} \\ &= \frac{w_{(S)}^1}{\sqrt{(w_{(S)}^1)^2 + (w_{(S)}^2)^2}}. \end{aligned} \quad (29)$$

The rotation angle  $\Theta$  is determined by

$$\begin{aligned} \sin \Theta &= \left[ \left( 1 - \sqrt{\frac{\Sigma \Delta}{-g_{tt} \mathcal{A}}} \right) \frac{\Gamma_{(Z)} w_{(Z)}^3}{1 + \Gamma_{(Z)}} + \frac{a \mathcal{B} \sin \theta}{\sqrt{-g_{tt} \Sigma \mathcal{A}}} \right] \\ &\quad \times \frac{\Gamma_{(Z)} \sqrt{\left( w_{(Z)}^1 \right)^2 + \left( w_{(Z)}^2 \right)^2}}{1 + \Gamma_{(S)}} \\ &= - \left[ \left( 1 - \sqrt{\frac{\Sigma \Delta}{-g_{tt} \mathcal{A}}} \right) \frac{\Gamma_{(S)} w_{(S)}^3}{1 + \Gamma_{(S)}} - \frac{a \mathcal{B} \sin \theta}{\sqrt{-g_{tt} \Sigma \mathcal{A}}} \right] \\ &\quad \times \frac{\Gamma_{(S)} \sqrt{\left( w_{(S)}^1 \right)^2 + \left( w_{(S)}^2 \right)^2}}{1 + \Gamma_{(Z)}}, \end{aligned} \quad (30)$$

and

$$\begin{aligned} \frac{\cos \Theta - 1}{1 - \sqrt{\frac{\Sigma \Delta}{-g_{tt} \mathcal{A}}}} &= \frac{\Gamma_{(Z)}^2 \left[ \left( w_{(Z)}^1 \right)^2 + \left( w_{(Z)}^2 \right)^2 \right]}{(1 + \Gamma_{(S)}) (1 + \Gamma_{(Z)})} \\ &= \frac{\Gamma_{(S)}^2 \left[ \left( w_{(S)}^1 \right)^2 + \left( w_{(S)}^2 \right)^2 \right]}{(1 + \Gamma_{(S)}) (1 + \Gamma_{(Z)})}. \end{aligned} \quad (31)$$

The frame  $E_\alpha(e, U)$  ( $E_\alpha(f, U)$ ) is obtained from  $E_\alpha(f, U)$  ( $E_\alpha(e, U)$ ) by a rotation with the angle  $\Theta$  ( $-\Theta$ ) about the axis  $\mathbf{n}$ . The rotation angle  $\Theta$  exists outside the ergosphere where the terms under the square roots in Equations (30) and (31) are positive. The transformation between  $E_\alpha(e, U)$  and  $E_\alpha(f, U)$  in another form is given in Appendix VII. The above transformation is a special case of the Wigner-rotation [102], which was discussed recently in Ref. [103]. However explicit expressions for the rotation between the frames which we denote  $E_\alpha(f, U)$  and  $E_\alpha(e, U)$  were not presented in [103].

### B. MPD spin equations in comoving and zero 3-momentum frames

We investigate two cases related to the chosen  $U$ -frame: *i*)  $U^a = p^a/M$  when we work in the zero 3-momentum frame; and *ii*)  $U^a = u^a$  which is the four velocity of the center of mass measured in the zero 3-momentum frame. In all cases the spin vector can be expanded as

$$S = S^\alpha E_\alpha, \quad (32)$$

since  $S^0 = 0$ . Here, the spatial frame vector  $E_\alpha$  in the  $U$ -frame denotes either  $E_\alpha(e, U)$  or  $E_\alpha(f, U)$ , which are obtained by boosting the SO and ZAMO frames, respectively.

The covariant derivative of the spin vector along the integral curve of  $u$  is

$$\frac{DS}{d\tau} = \frac{dS^\alpha}{d\tau} E_\alpha + S^\alpha \frac{DE_\alpha}{d\tau}. \quad (33)$$

Since the frame vectors are perpendicular to each other, we have

$$E_{\mathbf{A}} \cdot \frac{DE_{\mathbf{B}}}{d\tau} = -E_{\mathbf{B}} \cdot \frac{DE_{\mathbf{A}}}{d\tau}, \quad (34)$$

for  $\mathbf{A} \neq \mathbf{B}$ , and because of the normalization:

$$E_{\mathbf{A}} \cdot \frac{DE_{\mathbf{A}}}{d\tau} = 0. \quad (35)$$

Therefore the covariant derivatives of the spatial frame vectors along the integral curve of  $u$  can be expressed as

$$\frac{DE_\alpha}{d\tau} = - \left( E_0 \cdot \frac{DE_\alpha}{d\tau} \right) E_0 - \varepsilon_{\alpha\beta}{}^\gamma \Omega^\beta E_\gamma, \quad (36)$$

where  $\varepsilon_{\alpha\beta}{}^\gamma$  Levi-Civita symbol in the 3-dimensional Euclidean space, whose frame indices are raised and lowered by the 3-dimensional Kronecker  $\delta$ , and the frame components of the angular velocity are

$$\Omega^\alpha = -\frac{1}{2} \varepsilon^{\alpha\beta\gamma} E_\beta \cdot \frac{DE_\gamma}{d\tau}. \quad (37)$$

Due to Equation (34), the first term<sup>6</sup> in (36) can be written as

$$E_0 \cdot \frac{DE_\alpha}{d\tau} = -E_\alpha \cdot \mathbf{a}, \quad (38)$$

where  $\mathbf{a}$  denotes the acceleration  $\mathbf{a} = DE_0/d\tau$ . Now the spin Equation (33) becomes as

$$\frac{DS}{d\tau} = \left( \frac{dS^\alpha}{d\tau} + \varepsilon^\alpha_{\beta\gamma} \Omega^\beta S^\gamma \right) E_\alpha + (S \cdot \mathbf{a}) E_0. \quad (39)$$

Finally, we take into account the spin Equation (13). When considering the spin evolution in the zero 3-momentum frame, we find the following equation for the spin:

$$\frac{dS^\alpha}{d\tau} + \varepsilon^\alpha_{\beta\gamma} \Omega^\beta S^\gamma = 0. \quad (40)$$

The second case when considering the evolution of  $S^\alpha$  in the comoving frame, requires somewhat longer computation. Equations (13) and (39) results in

$$\left( \frac{dS^\alpha}{d\tau} + \varepsilon^\alpha_{\beta\gamma} \Omega^\beta S^\gamma \right) E_\alpha + \Upsilon = 0, \quad (41)$$

with

$$\Upsilon = \left[ (S \cdot \mathbf{a}) u^{\mathbf{A}} - (S \cdot \mathbf{F}) \frac{p^{\mathbf{A}}}{M^2} \right] E_{\mathbf{A}}. \quad (42)$$

<sup>6</sup> Note that this term vanishes when the first order spin corrections, i.e. the right hand sides of Equations (1) and (2), are neglected (see Ref. [92]).

Using Equations (6) and (12), a straightforward computation shows that  $u \cdot \Upsilon = 0$ . Therefore,  $\Upsilon$  can be expanded as  $\Upsilon = \Upsilon^\alpha E_\alpha$ . On the other hand  $\Upsilon$  is perpendicular to  $S$ , hence, we can introduce a vector  $\omega$ , whose frame components obey the relation

$$\varepsilon^\alpha_{\beta\gamma} \omega^\beta S^\gamma = \Upsilon^\alpha. \quad (43)$$

The vector  $\omega$  is determined ambiguously since its frame component parallel with  $S$  vanishes in the cross product. As a natural choice, we choose  $\omega$  to be perpendicular to  $S$ . Using the definition (43), Equation (41) reads as

$$\frac{dS^\alpha}{d\tau} + \varepsilon^\alpha_{\beta\gamma} (\Omega^\beta + \omega^\beta) S^\gamma = 0. \quad (44)$$

The Equations (40) and (44) can be considered in either the  $E_\alpha(e, U)$  or the  $E_\alpha(f, U)$  frame. Introducing the notations

$$k = \{e, f\}, \quad \Gamma = \{\Gamma_{(S)}, \Gamma_{(Z)}\}, \quad (45)$$

the angular velocity components  $\Omega^\alpha(k, U)$  can be determined by using

$$\begin{aligned} & E_\beta(k, U) \cdot \frac{DE_\alpha(k, U)}{d\tau} \\ &= k_\beta \cdot \frac{Dk_\alpha}{d\tau} \\ &+ \frac{1}{1+\Gamma} [(U \cdot k_\alpha) k_\beta - (U \cdot k_\beta) k_\alpha] \cdot \frac{Dk_0}{d\tau} \\ &+ \frac{1}{1+\Gamma} [(U \cdot k_\alpha) k_\beta - (U \cdot k_\beta) k_\alpha] \cdot \frac{DU}{d\tau}, \end{aligned} \quad (46)$$

where  $\alpha \neq \beta$ . This can be computed once  $U$  is determined.<sup>7</sup>

When both SO and ZAMO frames exist, a rotation about the axis  $\mathbf{n}$  defined by Equations (28) and (29) [see also Appendix VII for the explicit expressions] relates  $E_\alpha(f, U)$  to  $E_{\alpha'}(e, U)$  which can be written as

$$E_\beta(e, U) = \mathcal{R}^{\alpha'}_{\beta} E_{\alpha'}(f, U). \quad (47)$$

Here  $\mathcal{R}^{\alpha'}_{\beta}$  denotes the components of the corresponding rotation matrix. From the definitions of  $\Omega^\alpha(e, U)$  and  $\Omega^{\alpha'}(f, U)$ , the following relation between them can be derived:

$$\mathcal{R}^{\beta'}_{\alpha} \Omega^\alpha(e, U) = \Omega^{\beta'}(f, U) + \mathcal{R}^{\beta'}_{\alpha} \Omega^\alpha_{(\mathcal{R})}. \quad (48)$$

Here we have introduced  $\Omega^\gamma_{(\mathcal{R})}$  as

$$(\mathcal{R}^{-1})^\alpha_{\nu'} \frac{d\mathcal{R}^{\nu'}}{d\tau} = \varepsilon^\alpha_{\gamma\beta} \Omega^\gamma_{(\mathcal{R})}, \quad (49)$$

which is the angular velocity of rotation between the frame bases along the body's trajectory.

### 1. Cartesian-like triads and the characterization of spin evolution

The evolution of the spin vector can be illustrated suitably by comparison its direction with Cartesian axes which are fixed with respect to the distant stars. The static observers are those fiducial observers, whose frame does not move with respect to the black hole's asymptotic frame [104]. A static observer sees the same "nonrotating" sky during the evolution. In this sense the static observers are preferred fiducial observers in the investigation of spin dynamics. Following Ref. [92], we introduce a spatial Cartesian-like triad  $e_{\mathbf{x}}$ ,  $e_{\mathbf{y}}$  and  $e_{\mathbf{z}}$  in the local rest space of the static observer as  $e_\alpha = R^{\mathbf{i}}_{\alpha} e_{\mathbf{i}}$ , where  $\alpha = \{1, 2, 3\}$ ,  $\mathbf{i} = \{\mathbf{x}, \mathbf{y}, \mathbf{z}\}$  and  $R$  is the same rotation matrix, which relates the Cartesian and spherical coordinates in the 3-dimensional Euclidean space (see Equation (85) of [92]). Since the rotation  $R$  and the boost can be interchanged, we have  $E_\alpha(e, U) = R^{\mathbf{i}}_{\alpha} E_{\mathbf{i}}(e, U)$ .

The family of static observers only determines a frame outside the ergosphere. Therefore, we introduce another Cartesian-like triad  $f_{\mathbf{x}}$ ,  $f_{\mathbf{y}}$  and  $f_{\mathbf{z}}$  in the local rest space of ZAMO for representation of the spin evolution inside the ergosphere<sup>8</sup> as  $f_\alpha = R^{\mathbf{i}}_{\alpha} f_{\mathbf{i}}$ . Then the boost transformation results in  $E_\alpha(f, U) = R^{\mathbf{i}}_{\alpha} E_{\mathbf{i}}(f, U)$ .

The Cartesian-like triad components of the spin vector in both the boosted SO and ZAMO frames are obtained as

$$S^{\mathbf{i}} = R^{\mathbf{i}}_{\alpha} S^\alpha, \quad (50)$$

which obeys the following equation of motion:

$$\frac{dS^{\mathbf{i}}}{d\tau} = -R^{\mathbf{i}}_{\alpha} \varepsilon^\alpha_{\beta\gamma} \Omega^\beta_{(prec)} S^\gamma. \quad (51)$$

Here the precession angular velocity is<sup>9</sup>

$$\Omega^\beta_{(prec)} = \Omega^\beta_{(p)} + \epsilon \omega^\beta, \quad (52)$$

with

$$\Omega^\beta_{(p)} = -\Omega^\beta_{(orb)} + \Omega^\beta, \quad (53)$$

where  $\Omega^\beta_{(orb)}$  defined [see also Ref. [92]] as

$$(R^{-1})^\alpha_{\mathbf{j}} \frac{dR^{\mathbf{j}}}{d\tau} = \varepsilon^\alpha_{\gamma\beta} \Omega^\gamma_{(orb)}, \quad (54)$$

<sup>7</sup> We note that when the right hand sides of Equations (1) and (2) are neglected, the centroid moves along a geodesic, thus  $\omega$  and the last term in (46) vanish. The four-velocity  $U$  is determined from the geodesic equation, and for  $k = e$ , we obtain the same system which was investigated in Ref. [92].

<sup>8</sup> Note that the frame associated to the ZAMO moves with respect to the distant stars.

<sup>9</sup> Note that that the expression of  $\Omega^\beta_{(prec)}$  reduces to -1 times that of Ref. [92] for  $\epsilon = 0$ .

and  $\epsilon = 0$  in the zero 3-momentum frame, while  $\epsilon = 1$  in the comoving frame. The angular velocity  $\Omega_{(prec)}^\beta$  describes the spin precession in the Cartesian-like frame. The Cartesian-like triad components of  $\Omega_{(prec)}^\beta$  are obtained from Equation (50) with notation change  $S \rightarrow \Omega_{(prec)}$ .

The quantity  $\Omega_{(p)}$  can also be expressed in terms of the inner product of the Cartesian-like triad vectors  $E_i$  and their derivatives along the considered worldline as

$$\Omega_{(p)}^i \equiv R^\beta_i \Omega_{(p)}^\beta = -\frac{1}{2} \varepsilon^{ijk} E_j \cdot \frac{DE_k}{d\tau}. \quad (55)$$

This expression is analogous with Equation (37). The angular velocities  $\Omega_{(p)}^i(e, U)$  and  $\Omega_{(p)}^i(f, U)$  defined in terms of  $E_i(e, U)$  and  $E_i(f, U)$ , respectively, are related by

$$\begin{aligned} T^{\mathbf{k}'}_i \Omega_{(p)}^i(e, U) + S^{\mathbf{k}'}_\alpha \Omega_{(orb)}^\alpha(e, U) \\ = \Omega_{(p)}^{\mathbf{k}'}(f, U) + R^{\mathbf{k}'}_{(f)\beta} \Omega_{(orb)}^{\beta'}(f, U) + S^{\mathbf{k}'}_\alpha \Omega_{(\mathcal{R})}^\alpha, \end{aligned} \quad (56)$$

with

$$T^{\mathbf{k}'}_i \equiv \left(R_{(e)}^{-1}\right)_i^\beta \mathcal{R}_{\beta'}^{\alpha'} R^{\mathbf{k}'}_{(f)\alpha'}, \quad S^{\mathbf{k}'}_\alpha \equiv R^{\mathbf{k}'}_{(f)\beta'} \mathcal{R}_{\alpha'}^{\beta'}. \quad (57)$$

Noting that  $\omega^\alpha$  in Equation (43) transforms as a vector for real rotation  $\mathcal{R}_{\alpha'}^{\beta'}$ . The transformation rules for  $\Omega_{(prec)}^\beta$  and  $\Omega_{(prec)}^i$  follow from the definitions (52) and (56).

#### IV. NUMERICAL INVESTIGATIONS

The orbit of the spinning body will be represented in the coordinate space:

$$x = r \cos \phi \sin \theta, \quad y = r \sin \phi \sin \theta, \quad z = r \cos \theta. \quad (58)$$

We characterize the instantaneous plane of the motion in the  $(x, y, z)$ -space by the unit vector:

$$\mathbf{l} = \frac{\mathbf{R} \times \mathbf{V}}{|\mathbf{R} \times \mathbf{V}|}, \quad (59)$$

where  $\times$  is the cross product in Euclidean 3-space,  $\mathbf{R}$  is the position vector with components  $R^x = x$ ,  $R^y = y$ ,  $R^z = z$ , and  $\mathbf{V}$  is a spatial velocity vector with<sup>10</sup>

$$V^x = \frac{dx}{d\tau}, \quad V^y = \frac{dy}{d\tau}, \quad V^z = \frac{dz}{d\tau}. \quad (60)$$

The absolute value in the denominator denotes the “Euclidean length” of the numerator. Since the considered spacetimes are asymptotically flat, the quantity  $l^i$  coincides with the direction of the orbital angular momentum<sup>11</sup> at spatial infinity.

The initial data for the spin vector will be characterized by its magnitude and two angles in the boosted SO Cartesian-like frame as

$$S = S^i E_i(e, u), \quad (61)$$

with

$$S^i = |S| \left( \cos \phi^{(S)} \sin \theta^{(S)}, \sin \phi^{(S)} \sin \theta^{(S)}, \cos \theta^{(S)} \right). \quad (62)$$

Since we use dimensionless quantities during the numerical investigation, the parameters  $\mu$ ,  $a$ ,  $m$  and  $M$  only appear through the ratios  $a/\mu$  and  $m/M$ . We choose the initial data set in the TD SSC as  $p_{(TD)}^a/M$  and  $S^a/\mu M$  (by Equation (62)), then the initial spin tensor is derived from the inverse of (11), while  $m(0)/M(0)$  and the four velocity  $u_{(TD)}^a$  of the centroid from (6).

The SSC choice determining the representative worldline of a spinning test body corresponds to a gauge choice in an action approach [113]. In the following we will consider the evolution of the spin precessional angular velocity and will check its dependence on the SSC choice. For the numerical comparison, we will use the Frenkel–Mathisson–Pirani (FMP) SSC which imposes  $u_a S^{ab} = 0$ . The definition of the spin vector is  $s^a = -\eta^{abcd} u_b S_{cd}/2$ , which is Fermi–Walker transported along the worldline of the centroid making the FMP SSC preferred from mathematical point of view [114–116]. Its frame components obey the same precessional equation in the comoving frame like the TD spin vector  $S^a$  in the zero 3-momentum frame (13). In the FMP SSC, there exists also a velocity-momentum relation, Equation (19) of Ref. [97], like in the TD SSC. Hence the initial data set  $\{x^a, p^a, S^{ab}\}|_{\tau_{in}}$  provides a unique solution of the MPD equation with FMP SSC. However, we must mention that, this velocity-momentum relation does not automatically ensure that  $u_a S^{ab} = 0$  for arbitrary  $p^a$  and  $S^{ab}$ . In order to ensure this, we have a constraint between the four momentum and the spin tensor emerging from the contraction of this equation with  $S_{ab}$ . In addition, the data set  $\{x^a, p^a, S^{ab}\}|_{\tau_{in}}$  cannot be inverted for the set  $\{x^a, m, u^a, S^{ab}\}|_{\tau_{in}}$  like in the TD SSC. One needs the data set  $\{x^a, m, u^a, S^{ab}, a^a\}|_{\tau_{in}}$  to fix the trajectory. For a set  $\{x^a, m, u^a, S^{ab}\}|_{\tau_{in}}$ , we can obtain a non-helical and infinite number of helical trajectories for



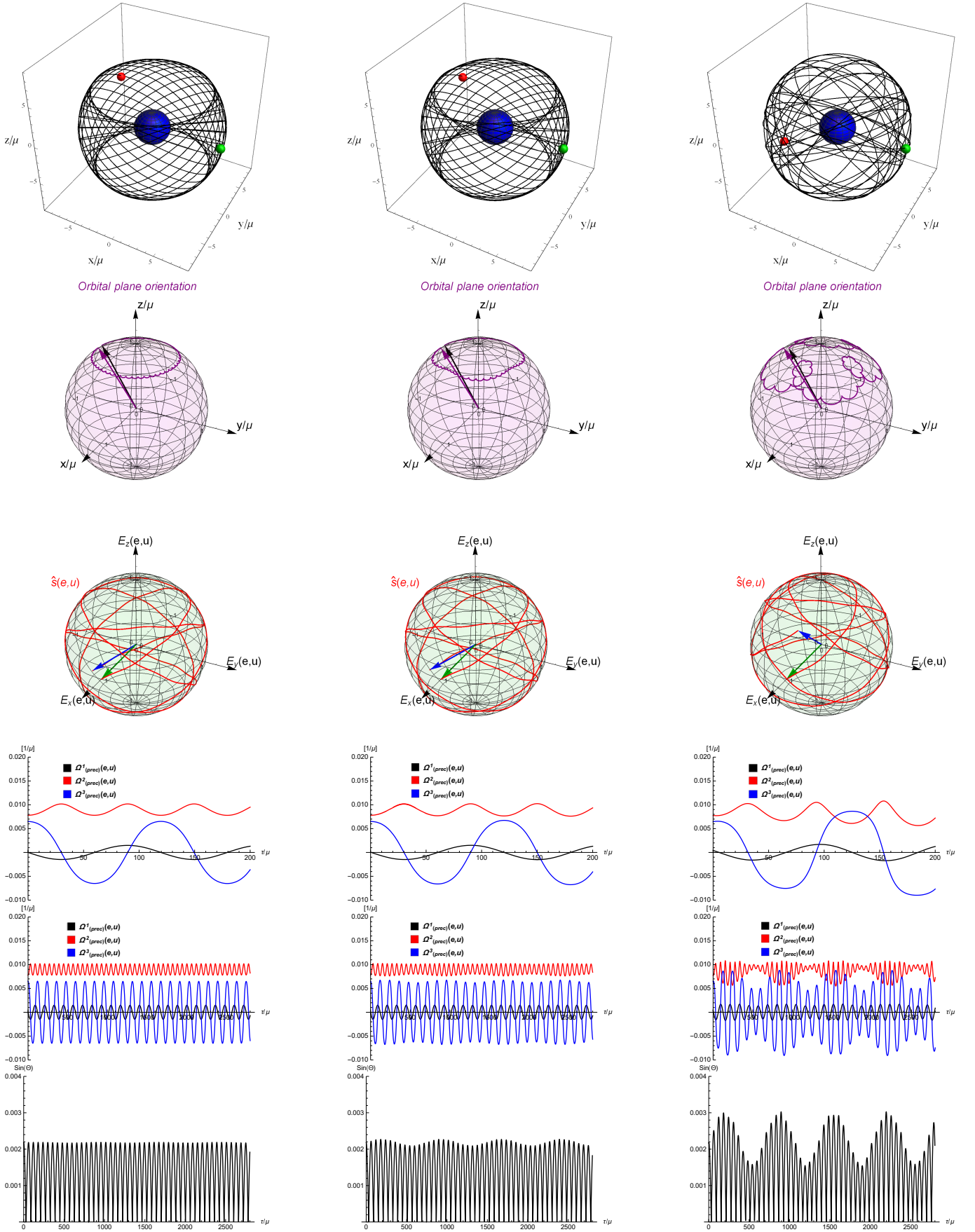


Figure 1: (color online). The evolution of spinning body moving on spherical-like orbits around the Kerr black hole with  $a = 0.5\mu$ . From left to right the magnitude of the body's spin increases as  $|S|/\mu M = 0.01, 0.1$  and  $0.9$ . The rows represent the following: 1. the orbit in coordinate space ( $x/\mu, y/\mu, z/\mu$ ) (the ergosphere of the central black hole is marked by blue and the initial and the final positions of the spinning body are denoted by green and red dots, respectively), 2. the instantaneous orbital plane orientation  $l^1$  (initial and final directions are marked by purple and black arrows, respectively), 3. unit spin vector in the boosted SO comoving Cartesian-like frame  $E_i(e, u)$  (initial and final spin directions are marked by green and blue arrows, respectively), 4. and 5.  $\Omega_{(prec)}^\alpha(e, u)$  on shorter and longer timescales, respectively, 6.  $\sin \Theta$ . The initial place of the body is  $r(0) = 8\mu$ ,  $\theta(0) = \pi/2$  and  $\phi(0) = 0$ . The direction of the initial spin vector is given by  $\theta^{(S)}(0) = \pi/2$  and  $\phi^{(S)}(0) = 0$  in the boosted SO frame (resulting in  $S^r(0)/|S| = 0.8682$ ,  $\mu S^\theta(0)/|S| = 0$  and  $\mu S^\phi(0)/|S| = 0$  in Boyer-Lindquist coordinates). The four momentum  $p_{(TD)}^a/M$  is chosen for the TD SSC as  $p_{(TD)}^r(0)/M(0) = 0$ ,  $\mu p_{(TD)}^\theta(0)/M(0) = 0.0442$  and  $\mu p_{(TD)}^\phi(0)/M(0) = -0.0316$ . The initial centroid four velocity  $u_{(TD)}^a$  is determined from Equation (6).

different  $a^a$ . In principle all worldlines where the conditions  $u_a u^a = -1$ ,  $u_a S^a = 0$  and  $p_a S^a = 0$  are satisfied can be used for representation of the moving body. Since the tangent vector of the centroid orbit occurs in the spin precessional equation through  $E_A$  and their derivatives, the spin axis may describe very complicated motion in such observer's frame, which follows a helical trajectory. In order to characterize the self rotation of the body in the easiest way possible, the helical trajectories should be avoided. However, there is no generic rule for determination of the non-helical trajectory. According to the Authors' knowledge, the best ansatz is suggested in Ref. [115] as taking

$$p^a = m u^a + S^{ab} \frac{F_b}{m}. \quad (63)$$

In this case  $a^a \propto F^a/m$  at leading order in spin, which is plausible for a non-helical trajectory since  $a^a \propto \mathcal{O}(S^{-1})$  for the helical ones. However, the ansatz (63) cannot be imposed as a constraint for the dynamics with significant spin magnitude in the consideration. We require the ansatz (63) for setting initial conditions in the numerical investigations. This is not forbidden because (63) is consistent with the algebraic velocity-momentum equation. The corresponding initial data set in the FMP SSC are chosen by identifying the initial centroid four velocity and spin vector as  $u_{(FMP)}^a = u_{(TD)}^a$  and  $s^a/m = S^a/M$ . Then the initial spin tensor and  $p_{(FMP)}^a/m$  are computed from  $S^{ab} = \eta^{ab}_{cd} u^c s^d$  and (63), respectively. Bringing forward the result of the SSC dependence, we have found that the evolutions of the spin vectors defined in the TD and the FMP SSCs are barely distinguishable from each other in all cases. The differences in the evolutions of the different considered quantities considered in the subsequent subsections remains below 1%. This is in agreement with result of Ref. [117], where the evolution of test bodies moving on circular equatorial orbits around a Schwarzschild black hole were investigated.

### A. Spinning bodies moving in the Kerr spacetime

In this subsection, we set  $\mu_{em} = 0$  and  $a/\mu < 1$ , i.e. the background is a Kerr black hole's spacetime. Figure 1 shows spherical-like orbits. The initial values are listed in the caption. The orbits, the black curves in the upper row, are shown in the coordinate space  $(x/\mu, y/\mu, z/\mu)$  defined in Equation (58). The initial and the final positions of the body are marked by green and red dots, respectively. The initial position is in the equatorial plane  $\theta(0) = \pi/2$  at  $r(0) = 8\mu$  and  $\phi(0) = 0$ . The blue surface at the center depicts the outer bound of the Kerr black hole's ergosphere. In the columns from left to right, the spin magnitude  $|S|/\mu M$  variates as 0.01, 0.1 and 0.9, respectively, while the other initial values are fixed. For small spin, the orbit is spherical ( $\dot{r} = 0$ ) and reproduces Figure 3 of [92]. For higher spins (second

and third columns) the orbit becomes less and less spherical, but because of  $\dot{r} \ll 1$ , it is spherical-like. On the purplish spheres in the second row, the evolutions of the kinematical quantity defined in Equation (59) are shown under the corresponding orbits. Their initial and final directions are marked by purple and black arrows, respectively. The evolution of this vector clearly shows that the increasing spin magnitude due to the nonvanishing spin-curvature coupling (i.e. the non-vanishing right hand side of Equation (1)) in the spin precession, which was not included in the investigation of Ref. [92]) affects the orbit. On the greenish spheres in the third row, the evolutions of the spin direction are represented in the boosted SO frame  $E_i(e, u)$ . The initial and final spin directions are marked by green and blue arrows, respectively. In Boyer-Lindquist coordinates, the initial spin four vector  $S^a$  has only non-vanishing component  $S^r$ . The fourth and fifth rows image the evolutions of spin precessional angular velocity  $\Omega_{(prec)}^\alpha(e, u)$  on shorter and longer timescales, respectively. For  $|S|/\mu M = 0.01$ , the frame components of this angular velocity oscillates (see also Figure 3 of Ref. [92] and remembering for that the definition of  $\Omega_{(prec)}^\beta$  carries an extra sign). For  $|S|/\mu M = 0.1$  and 0.9, an amplitude modulation occurs. This is also a clear sign of the spin-curvature effect. We mention that, the evolution of  $\Omega_{(prec)}^\alpha(f, u)$  differs less than 1% from that of  $\Omega_{(prec)}^\alpha(e, u)$ . This is because the boosted SO and ZAMO frames are almost the same, i.e. the rotation angle  $\Theta$  between them is small as shown in the last row. We also mention that, all precessional angular velocities  $\Omega_{(prec)}^\alpha(e, p/M)$ ,  $\Omega_{(prec)}^\alpha(e, u)$ ,  $\Omega_{(prec)}^\alpha(f, p/M)$  and  $\Omega_{(prec)}^\alpha(f, u)$  in the frames  $E_\alpha(e, p/M)$ ,  $E_\alpha(e, u)$ ,  $E_\alpha(f, p/M)$  and  $E_\alpha(f, u)$ , respectively, describe the same evolutions within 1%. The Boyer-Lindquist components of the spin vector are frame independent quantities. Their evolutions are presented on Figure 2. The blue, the green and the red curves belong to the different spin magnitude cases  $|S|/\mu M = 0.01$ ,  $|S|/\mu M = 0.1$  and  $|S|/\mu M = 0.9$ , respectively. An amplitude modulation due to the spin-curvature coupling occurs in the oscillation around a harmonic evolution of the  $\theta$ -component, which can be mostly seen along the red curve.

In the following, we will consider zoom-whirl and unbound orbits passing over the ergosphere. In all cases we choose such initial conditions that the body moves in the equatorial plane for negligible spin magnitude. Hence the deviation of the trajectory from this plane is a clear sign of the spin-curvature effect. Zoom-whirl orbits of a nonspinning test body around a spinning black hole were already investigated in Refs. [69–73]. Those orbits did not passed through the ergosphere for which we will focus. In addition, when the test body is spinning, some effects from the spin-curvature coupling are waited which we will consider. In addition, zoom-whirl orbits of comparable mass black holes, when only one of them is spinning, were analyzed in Ref. [80] within the framework of PN approximation. Hyperbolic orbits of spinning

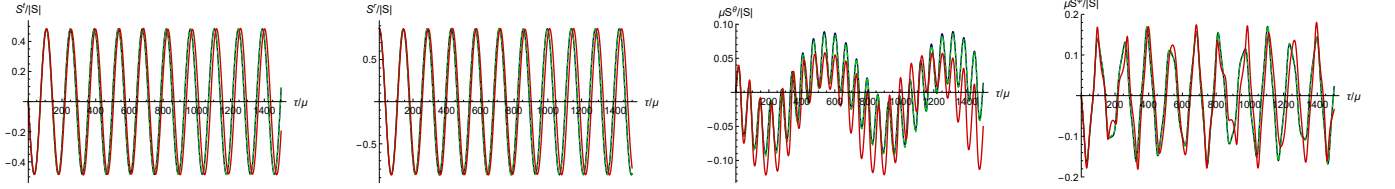


Figure 2: (color online). The evolutions of the Boyer-Lindquist coordinate components of the unit spin vector are shown. The blue and the green curves belonging to the spin magnitude  $|S|/\mu M = 0.01$  and  $|S|/\mu M = 0.1$ , respectively, almost cover each other. The red curve represents the high spin magnitude case  $|S|/\mu M = 0.9$ . An amplitude modulation occurs in the oscillation around a harmonic evolution of the  $\theta$ -component which can be mostly seen along the red curve.

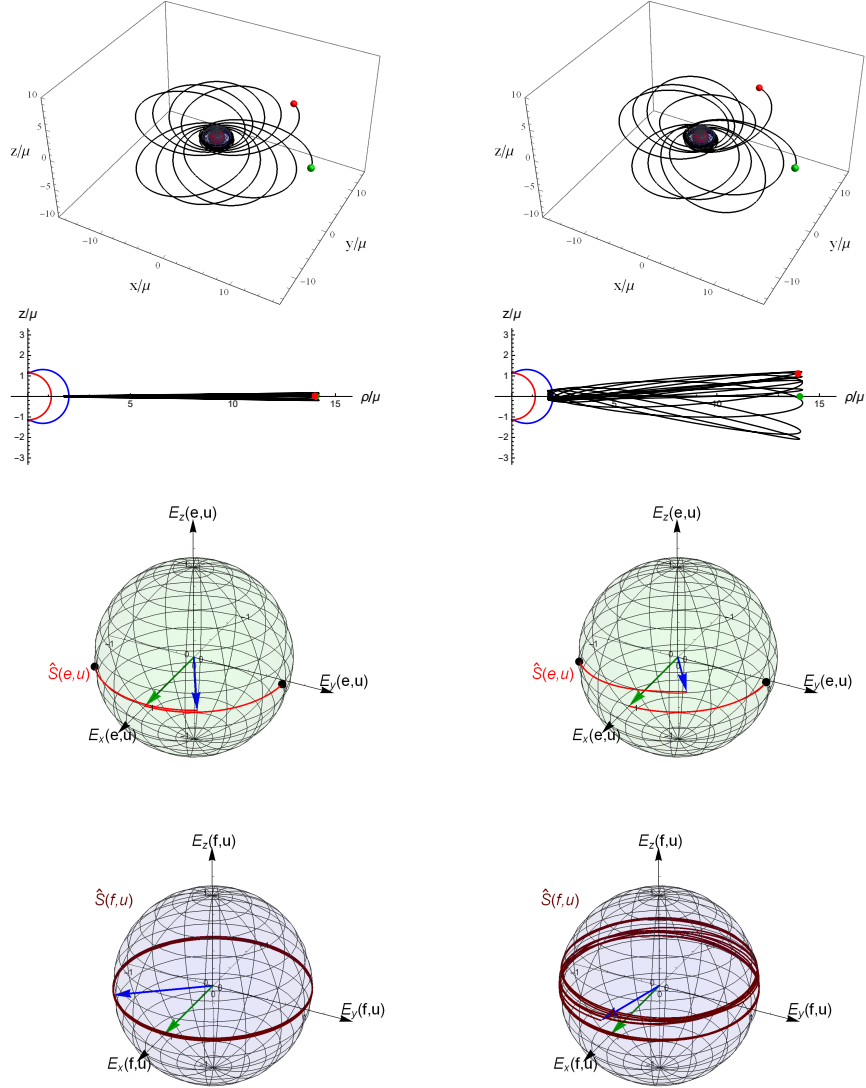


Figure 3: (color online). The evolution of spinning body moving on zoom-whirl orbits around the Kerr black hole with  $a = 0.99\mu$ . The magnitudes of the body's spin are  $|S|/\mu M = 0.01$  (left panel) and  $0.1$  (right panel). The rows represent the following: 1. the orbit in coordinate space  $(x/\mu, y/\mu, z/\mu)$  (outer and inner bounds of the ergosphere of the central black hole is marked by blue and red surfaces, respectively), and initial and final positions of the spinning body are denoted by green and red dots, respectively, 2. the orbit in the coordinate space  $\rho/\mu = r \sin \theta/\mu$  and  $z/\mu = r \cos \theta/\mu$  with marked initial and final positions and bounds of the ergosphere, 3. the unit spin vector in the boosted SO Cartesian-like comoving frame  $E_i(e, u)$  on a shorter timescale including the first whirling period, and 4. the unit spin vector in the boosted ZAMO Cartesian-like comoving frame  $E_i(f, u)$  on the total timescale (initial and final spin directions are marked by green and blue arrows, respectively). The initial data set:  $t(0) = 0$ ,  $r(0) = 14.05\mu$ ,  $\theta(0) = \pi/2$ ,  $\phi(0) = 0$ ,  $p^r(0)/M = -0.03$ ,  $\mu p^\theta(0)/M = 0$ ,  $\mu p^\phi(0)/M = 0.012$ ,  $\theta^{(S)}(0) = \pi/2$  and  $\phi^{(S)}(0) = 0$  (the spatial Boyer-Lindquist coordinate components are  $S^r(0)/|S| = 0.9293$ ,  $\mu S^\theta(0)/|S| = 0$  and  $\mu S^\phi(0)/|S| = -0.0002$ ).

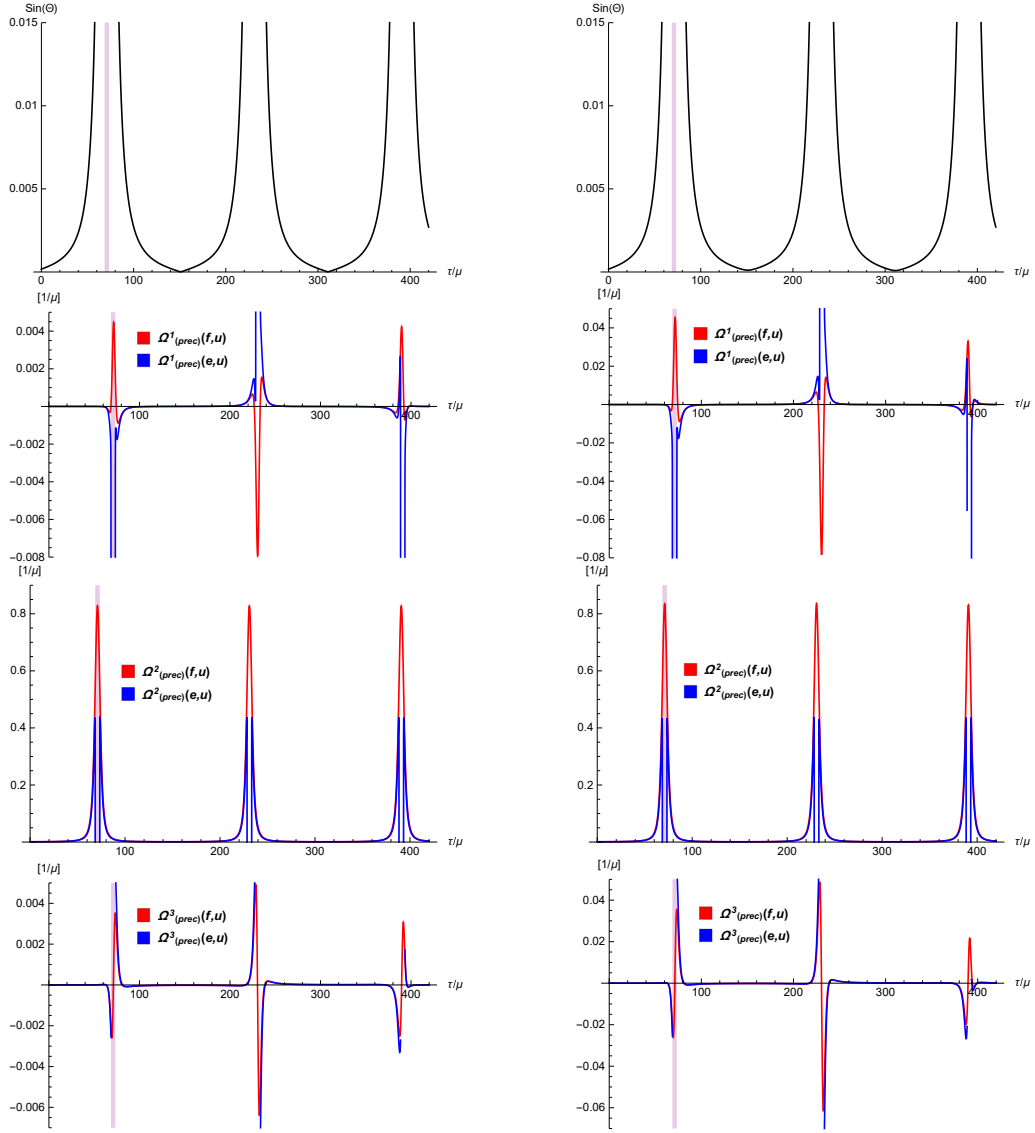


Figure 4: (color online). The left and right columns belong to the same evolution which are shown on Figure 3. The first row shows  $\sin \Theta$ . The next three rows present the evolutions of the spherical triad components of the spin precessional angular velocities  $\Omega_{(prec)}^\alpha(e, u)$  and  $\Omega_{(prec)}^\alpha(f, u)$ .

test bodies based on the MPD equations were analytically studied in Ref. [83]. The perturbations caused by the spin-curvature coupling in the equatorial orbits were considered in the case when the spin is parallel to the central black hole rotation axis. In this configuration the spin vector is conserved. Here, in order to discuss non-trivial spin evolution and spin-curvature coupling effects, we choose the initial spin direction to be perpendicular to the central black hole rotation axis.

The first row of Figure 3 shows the orbits in the  $(x, y, z)$ -space for increasing spin magnitude  $|S|/\mu M = 0.01$  (left panel) and  $0.1$  (right panel). The other initial values listed in the caption are the same. The blue and red surfaces at the center depict the outer and interior bounds of the ergosphere, respectively (i.e. the outer stationary

limit surface and the outer event horizon). The initial and final positions of the body are marked by green and red dots, respectively. The initial position is in the equatorial plane  $\theta(0) = \pi/2$  at  $r(0) = 14.05\mu$  and  $\phi(0) = 0$ , and both the initial four momentum and centroid four velocity have vanishing  $\theta$ -component. With this initial location and four velocity a non-spinning particle moves in the equatorial plane. However, since the spin direction is not parallel with the rotation axis of the central black hole, the body's centroid leaves the equatorial plane due to the effect of spin-curvature coupling. This is highlighted in the second row representing the orbits in coordinates  $\rho/\mu = r \sin \theta/\mu$  and  $z/\mu = r \cos \theta/\mu$ . The bounds of the ergosphere are drawn by blue and red curves. The body is inside the ergosphere when it whirls around the

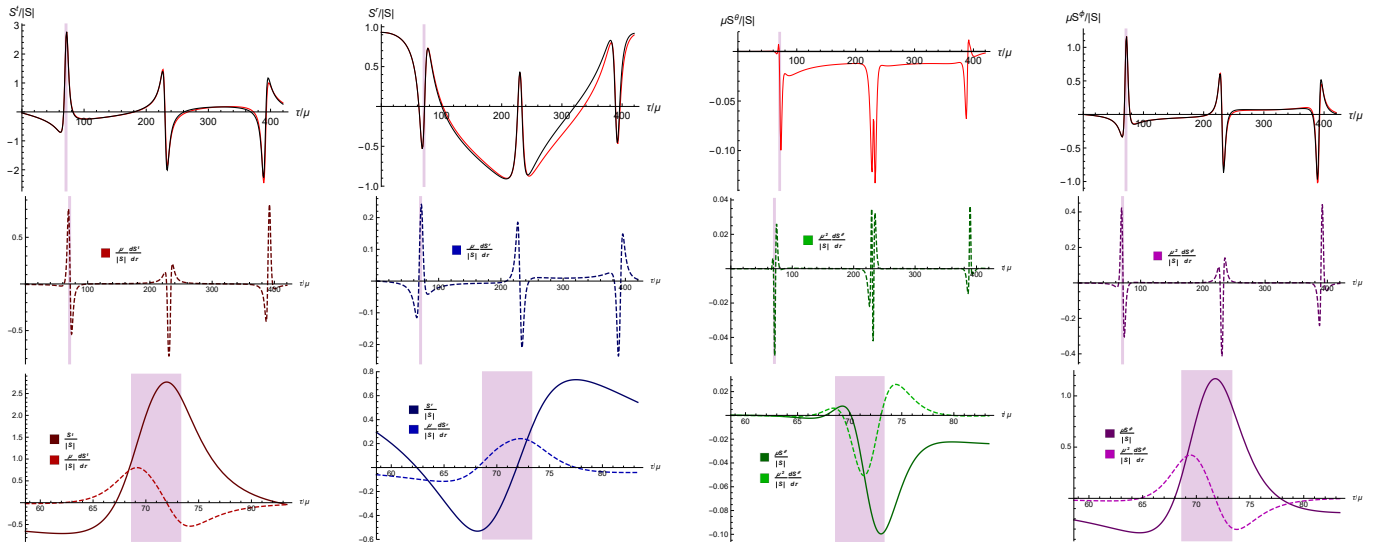


Figure 5: (color online). The evolution of the Boyer-Lindquist coordinate components of the unit spin vector and their derivatives rescaled to dimensionless variables is presented for that case which is shown on the right hand sides of Figures 3 and 4. The first and the second rows show the evolution on a timescale which includes the first three whirling period when the body is inside the ergosphere. The third row zooms in on that evolution period where the body is first in the ergosphere which is indicated by the purplish shadow on all panels. In the first row, the black and the red curves represent the evolutions without and with spin-curvature coupling, respectively.

central Kerr black hole. This happens during all whirling period. The unit spin vector evolutions in the boosted SO Cartesian-like comoving frame ( $E_i(e, u)$ ) during a timescale including the first whirling period are shown in the third row. The initial and final directions are marked by green and blue arrows, respectively. The rotation of the projection of spin vector in the plane ( $E_x(e, u)$ ,  $E_y(e, u)$ ) is counterclockwise in both cases. In the boosted SO frame the evolution is not continuous due to the motion through the ergosphere. The black dots denote the spin directions when the body first enters and leaves the ergosphere. The magnitude of the jump shows that the spin direction changed significantly inside the ergosphere. The fourth row shows the unit spin vector evolution on the total timescale in the boosted ZAMO Cartesian-like comoving frame ( $E_i(f, u)$ ). This frame can be used for the spin representation inside the ergosphere, hence the evolution is continuous. For higher spin, when the spin-curvature coupling is stronger the deflection of the spin direction moves more out of the equatorial plane of ZAMO frame. The first row in Figure 4 shows the rotation angle  $\Theta$  between the boosted SO and ZAMO frames. Here and in the following pictures the purplish shadow indicates the time interval where the body moves inside the ergosphere during the first whirling period. The next three rows in Figure 4 depict the evolutions of  $\Omega_{(prec)}^\alpha(e, u)$  and  $\Omega_{(prec)}^\alpha(f, u)$ . Each row shows one component of these angular velocities. The red and blue curves represent the precessional angular velocities in the boosted ZAMO and SO frames, respectively. The blue curves diverge at the ergosphere where the description in the

boosted SO frame fails. The magnitude of the precessional angular velocities rapidly increases near and inside the ergosphere and becomes higher for higher spin magnitude. Finally, we note that the precessional velocities  $\Omega_{(prec)}^\alpha(e, p/M)$  ( $\Omega_{(prec)}^\alpha(f, p/M)$ ) and  $\Omega_{(prec)}^\alpha(e, u)$  ( $\Omega_{(prec)}^\alpha(f, u)$ ) describe the same evolutions within 1%.

From the consideration of the moving body near and inside the ergosphere, we have found that the spin precession was highly increased. Since the presented investigation was based on the introduction of ZAMO, and the precessional angular velocity  $\Omega_{(prec)}^\alpha(f, u)$  described the spin evolution with respect to the boosted ZAMO frame, the highly increased precession effect could be an observer dependent statement. However, this effect is supported in another way. The static observers play fundamental role in comparing the variation of spin direction with respect to the distant stars. The third row of Figure 3 shows in the boosted SO frame that the jump of the spin direction (between the black dots) happening during that period when the body is staying first in the ergosphere. This jump happens during relatively short period indicated by the purplish shadow on Figure 4. More exactly, the evolution period presented in the third row of Figure 3 is given by  $\tau = [0, 94.7\mu]$  from which the body is inside the ergosphere in the interval  $\tau = [68.6\mu, 73.4\mu]$ . The evolution of the spin together with these timescales result in the same conclusion that the precession angular velocity is highly increased in the ergosphere. In addition, this effect can also be supported without using any particular reference frame. For the case presented on the right hand side of Figure 4, we show the evolution of the Boyer-Lindquist coordinate components of the unit

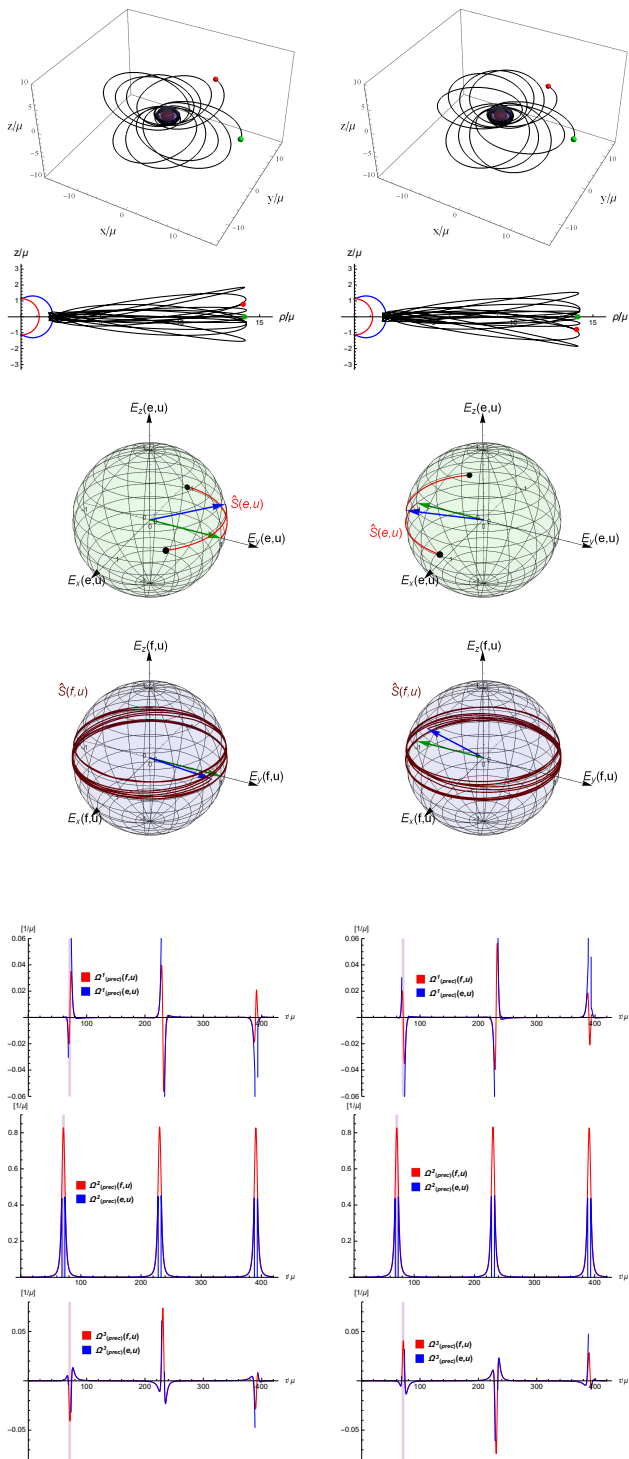


Figure 6: (color online). The same as on the right column of Figures 3 and 4 (apart from  $\sin \Theta$ ), but the initial direction of the spin vector is rotated by  $\pi/2$  (left column) and by  $-\pi/2$  (right column). (The spatial Boyer-Lindquist coordinate components of the spin vector are  $S^r(0)/|S| = -0.0025$  (left column),  $0.0025$  (right column),  $\mu S^\theta(0)/|S| = 0$  (both left and right columns) and  $\mu S^\phi(0)/|S| = 0.0720$  (left column),  $-0.0720$  (right column).

spin vector and their derivatives rescaled to dimensionless variables on Figure 5. The first and the second rows represent the evolution on a timescale which includes the first three whirling period when the body is

inside the ergosphere. The third row zooms in on that evolution period where the body is first inside the ergosphere. As mentioned, this period is indicated by the purplish shadow. All panels of Figure 5 confirm that the rate of change in the direction of the spin vector is highly increased near and inside the ergosphere. As a reference, the black curves in the first row represent the evolution of the unit spin coordinate components when the spin-curvature coupling is turned off. While the red curves show the evolutions when the spin-curvature coupling is taken into account. Significant differences in the evolutions can be seen in the case of the  $r$  and  $\theta$  coordinate components. The  $\theta$  coordinate component identically vanishes when the spin-curvature coupling is neglected. Finally, we mention that since  $p^a$  and  $u^a$  are not parallel with each other it may happen that  $u^a u_a = 0$  [51, 66–68] or  $p_a u^a = 0$  [118–120]. The first case was discussed previously in Section IIA. The second case is equivalent with becoming the momentum light-like  $p_a p^a = 0$ , which can be seen from the contraction Equation (6) with  $p_a$ . We have checked in the Appendix VIII that the MPD equations are applied only in that domain where such pathological behaviours do not occur.

When the initial direction of the spin vector is opposite with respect to the case presented in the Figures 3 and 4, while all other initial conditions are the same, we have found the following. The centroid trajectory becomes the reflection of the orbit presented on Figure 3 through the equatorial plane. The instantaneous directions of the spin vector in the boosted SO (ZAMO) frame can be obtained from the corresponding picture of Figure 3 by a rotation with an angle  $\pi$  about the axis  $z$  and  $E_z(e, u)$  ( $E_z(f, u)$ ), respectively. The angle  $\Theta$  describes the same evolution. Finally, the components  $\Omega_{(prec)}^2(e, u)$  and  $\Omega_{(prec)}^2(f, u)$  remain unchanged, while  $\Omega_{(prec)}^1(e, u)$ ,  $\Omega_{(prec)}^1(f, u)$ ,  $\Omega_{(prec)}^3(e, u)$  and  $\Omega_{(prec)}^3(f, u)$  get an extra sign.

On Figure 6, the initial spin direction is rotated by  $\pi/2$  (left column) and  $-\pi/2$  (right column) in the plane  $(E_x(e, u), E_y(e, u))$  with respect to the case presented on Figure 3. These two cases have opposite initial spin directions leading to the following differences in the orbit and spin evolutions. The zoom-whirl orbit on the right hand side is the reflection of the trajectory on the left hand side through the equatorial plane, which are shown in the first two rows. The spin the evolutions presented on the left and the right hand sides in the third and fourth rows are related to each other by a rotation with an angle  $\pi$  about the axis connecting the south and north poles. The evolution of  $\Omega_{(prec)}^2$  are the same on the left and right hand sides, while  $\Omega_{(prec)}^1$  and  $\Omega_{(prec)}^3$  have a sign difference, as it can be seen in the last three rows.

For the consideration of evolutions of spinning bodies which follow unbound orbits crossing through the ergosphere, the spin magnitude is chosen as  $|S|/\mu M = 0.1$ . The initial spin directions on the left (right) hand side of Figure 7 are the same as on Figure 3 (on the left hand



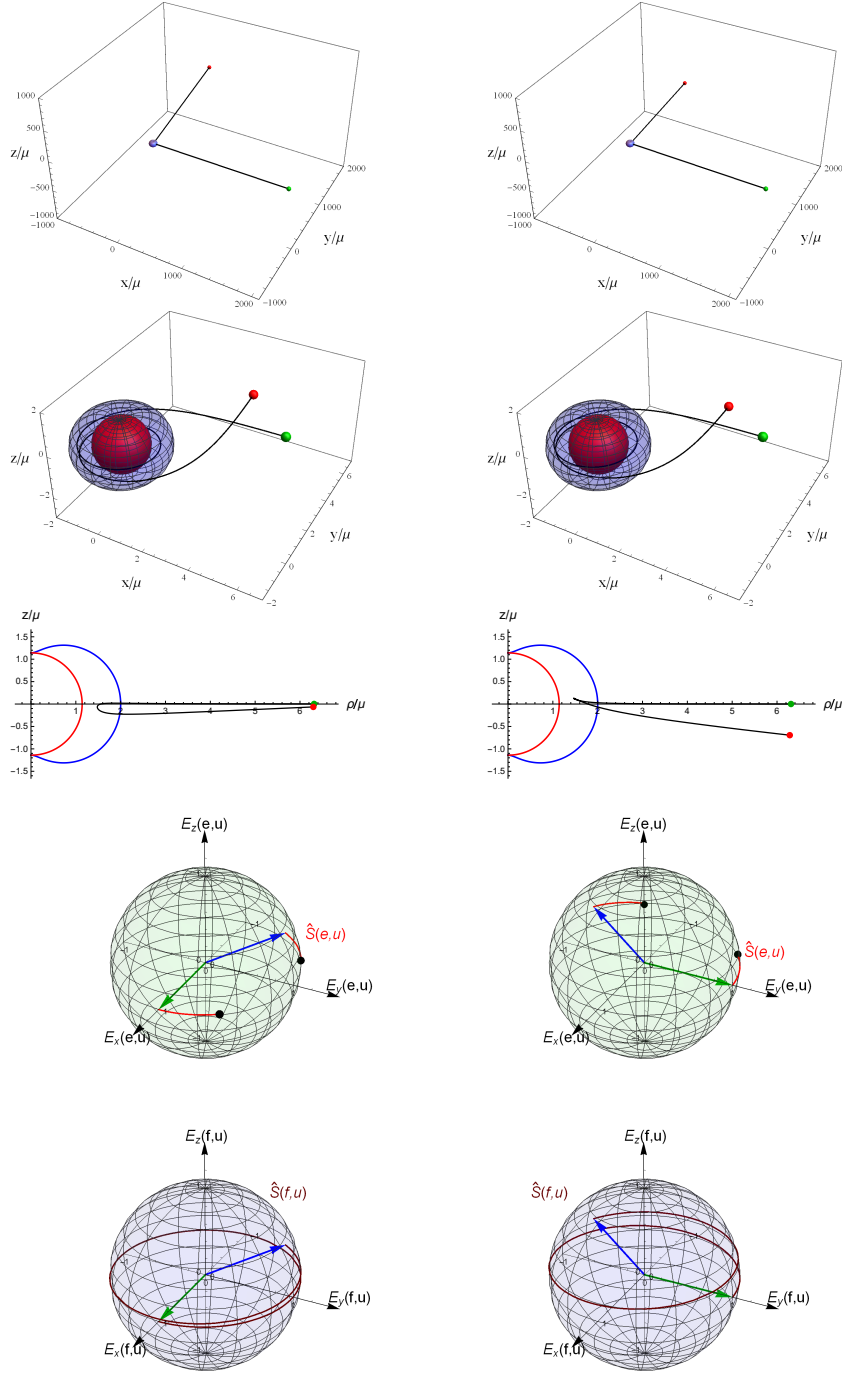


Figure 7: (color online). The evolutions of spinning body moving on unbound orbits around Kerr black hole with  $a = 0.99\mu$ . The spin magnitude chosen as  $|S|/\mu M = 0.1$ . The considered unbound orbits are shown in the first row. The near black hole parts of these orbits are represented in the second and third rows in  $(x/\mu, y/\mu, z/\mu)$  and  $(\rho/\mu, z/\mu)$  coordinates, respectively. The fourth and fifth rows present the evolutions of the spin vector in the boosted SO and ZAMO frames, respectively. The initial spin direction is determined by  $\phi^{(S)}(0) = 0$  (left col.),  $\pi/2$  (right col.) and  $\theta^{(S)}(0) = \pi/2$  (both cols.). The spatial Boyer-Lindquist coordinate components  $[S^r(0), \mu S^\theta(0), \mu S^\phi(0)]/|S|$  of the spin vector are  $[-0.0134, 0, -3.1 \times 10^{-9}]$  and  $[-0.000006, 0, 0.000005]$  in the left and right columns, respectively. Additional initial data set is  $t(0) = 0$ ,  $r(0) = 2000\mu$ ,  $\theta(0) = \pi/2$ ,  $\phi(0) = 0$ ,  $p^r(0)/M = -0.9$ ,  $\mu p^\theta(0)/M = 8 \times 10^{-7}$  and  $\mu p^\phi(0)/M = 0$ . The final locations  $[t(\tau^*)/\mu, r(\tau^*)/\mu, \theta(\tau^*), \phi(\tau^*)]$  at  $\tau^* = 4433\mu$  are  $[6033.2, 1999.7, 1.527, 14.24]$  (left col.) and  $[6033.3, 1999.7, 1.671, 14.25]$  (right col.). The final values of the spatial Boyer-Lindquist components  $[p^r(\tau^*), \mu p^\theta(\tau^*), \mu p^\phi(\tau^*)]/M$  of the four momentum are  $[0.900002, -7.65 \times 10^{-8}, 8.00 \times 10^{-7}]$  (left col.) and  $[0.900003, -3.48 \times 10^{-8}, 8.01 \times 10^{-7}]$  (right col.). The final values of the spatial Boyer-Lindquist components  $[S^r(\tau^*), \mu S^\theta(\tau^*), \mu S^\phi(\tau^*)]/|S|$  of the spinvector are  $[0.86, -2.9 \times 10^{-5}, 3.8 \times 10^{-4}]$  (left col.) and  $[-1.11, -8.6 \times 10^{-5}, 2.7 \times 10^{-4}]$  (right col.). The final spin directions  $[\theta^{(S)}(\tau^*), \phi^{(S)}(\tau^*)]$  in the boosted SO frame are determined by  $[1.48, -0.59]$  (left col.) and  $[1.31, 1.09]$  (right col.). The angles  $[\theta^{(l)}(\tau^*), \phi^{(l)}(\tau^*)]$  characterizing the final orbital plane orientations in coordinate space  $(x/\mu, y/\mu, z/\mu)$  are  $[0.11, -0.33]$  (left col.) and  $[0.11, 1.27]$  (right col.).

side of Figure 6). The first row depicts the unbound orbits in the  $(x, y, z)$ -space. The initial data set is chosen at  $r(\tau = 0) = 2000\mu$  where the body is in the equatorial plane ( $\theta(\tau = 0) = \pi/2$  and  $\phi(\tau = 0) = 0$ ) and the centroid four velocity has vanishing  $\theta$ -component. We numerically checked that  $r \rightarrow \infty$  as  $\tau \rightarrow \pm\infty$ . Second and third rows represent the orbits near the black hole in the  $(x, y, z)$  and the  $(\rho, z)$  spaces, respectively. The interval for  $\tau$  is determined by  $-5\mu$  before and  $+5\mu$  after the body crossed the outer stationary limit surface. As the body penetrates the ergosphere, it makes two turns around the black hole, then it leaves the ergosphere going to the spatial infinity. These evolutions describe such scattering processes where the center is extremely approached. The deviation of the trajectory from the equatorial plane is an effect of the spin-curvature coupling. The fourth and fifth rows image the evolutions of the unit spin vector represented in the boosted SO and ZAMO frames, respectively. The deviation of the spin vector direction from the equatorial plane also occurs because of the spin-curvature coupling. The jump in the evolution of the spin vector in the boosted SO frame (marked by black dots) shows that the variation of spin direction takes place mainly inside the ergosphere. The large part of the variation of spin direction happens during that period when the body is inside the ergosphere. This time interval is  $\tau \in [2214.8\mu, 2218.6\mu]$  which is short with respect to the considered total evolution period  $\tau = [0, 4433\mu]$ . The final value of the proper time  $\tau^* = 4433\mu$  was chosen in such a way, that for  $\tau > \tau^*$  the spin angles undergo only insignificant changes. Figure 8 presents the evolutions of  $\Omega_{(prec)}^\alpha(e, u)$  and  $\Omega_{(prec)}^\alpha(f, u)$  for that time interval which is determined by  $-25\mu$  before and  $+25\mu$  after the body crossed the outer stationary limit surface. The purplish shadow denotes that period when the body is inside the ergosphere where the spin precessional angular velocity components increases.

The spin-curvature coupling mainly influences the smaller components of the precessional angular velocity  $\Omega_{(prec)}^1(f, u)$  and  $\Omega_{(prec)}^3(f, u)$ , as it can be seen in the first row of Figure 9. The black curve represents the evolutions without the spin-curvature coupling. In the case of the red curves, the spin-curvature coupling is taken into account, and they are the same as in the second column of Figure 8. The spin-curvature coupling increases the amplitude of the precessional angular velocity components.

The reparametrization invariance of the representative worldline also implies a gauge freedom [121]. Usually, the following choices for this timelike parameter are applied in the literature: *i*) the proper time ( $u^a u_a = -1$ ) [51, 92] also used in this paper; *ii*) the parameter determined by the normalization  $u_a p^a / M = -1$  [122, 123]; *iii*) the coordinate time  $t$  [96, 124]. Employing the TD SSC, considerable differences were not found in both the orbit and the spin dynamics when using the parameters either *i*) or *ii*) [64]. The orbit and the spin evolutions are unaffected when using the coordinate time  $t$  instead of the proper time  $\tau$ . However, the precessional angular

velocity is changed for  $\Omega_{(prec)}^\alpha / u^0$  which is shown in the second row of Figure 9 as a function of  $t$ . The black and the red curves represent the evolution without and with the spin-curvature coupling. We can conclude the same effects when we have considered the spin evolution with respect to the proper time.

The relatively rapid change in the direction of the spin vector can also be confirmed without using any particular reference frame. In the first row of Figure 10, we present the evolutions of the Boyer-Lindquist coordinate components of the unit spin vector for the case imaged on the right hand sides of Figures 7 and 8. The spin-curvature coupling is included in the evolutions depicted by the red curves. The black curves represent the corresponding evolutions when this coupling is turned off. The effect of the spin-curvature coupling can be seen in the evolution of  $S^t$ ,  $S^r$  and  $S^\theta$  components. The latter vanishes identically in the absence of the spin-curvature coupling. However, if the spin-curvature coupling is included in the analysis, the  $S^\theta$  component deviates significantly from zero when the body is close to the central black hole. In addition, the effect of the spin-curvature coupling remains in the  $S^t$  and  $S^r$  components far from the central black hole. They approach another constant values when the spin-curvature coupling is taken into account. The evolutions of the components of the unit spin vector and their derivatives rescaled to dimensionless variables on a smaller timescale, when the spinning test body is close the central black hole are represented in the second row. All panels supports a relatively rapid change of the spin vector near and inside the ergosphere. Finally, we mention that the MPD equations were applied only in its validity domain, this check is given in the Appendix VIII.

In a wider range of initial conditions, the final values of the polar  $\theta^{(S)}$  and azimuthal  $\phi^{(S)}$  spin angles (the scattering angles) are represented on Figure 11 as functions of gauge invariant, dimensionless energy  $\hat{E} = E/M$  and angular momentum  $\hat{J}_z = J_z/\mu M$ . The small black dots in the plane of the initial spin angles ( $\theta^{(S)}(0) = \pi/2$  and  $\phi^{(S)}(0) = 0$ ) indicate the region, where the body crosses the event horizon of the Kerr black hole. Then, instead of a scattering process, the body falls into the black hole. Close to the left corner, i.e. at smaller  $\hat{E}$  and higher  $\hat{J}_z$  values, the body approaches the central black hole less than for higher  $\hat{E}$  and/or for smaller  $\hat{J}_z$  values. As a consequence, the precession and hence the variation of the spin angles are both small. However, close to the diagonal in the  $\hat{E}$ ,  $\hat{J}_z$  plane indicated by the edge of the black dots region, the body enters into the ergosphere, and due to the high precession there, the spin angles undergo a relatively large change. In all case, the initial values are chosen such that, if the spin-curvature coupling is neglected, the polar angle  $\theta^{(S)}$  remains  $\pi/2$  during the whole evolution, and the spin precession influences only  $\phi^{(S)}$ . Hence, the variation of  $\theta^{(S)}$  shown on the left panel is a clear effect of the spin-curvature coupling. We



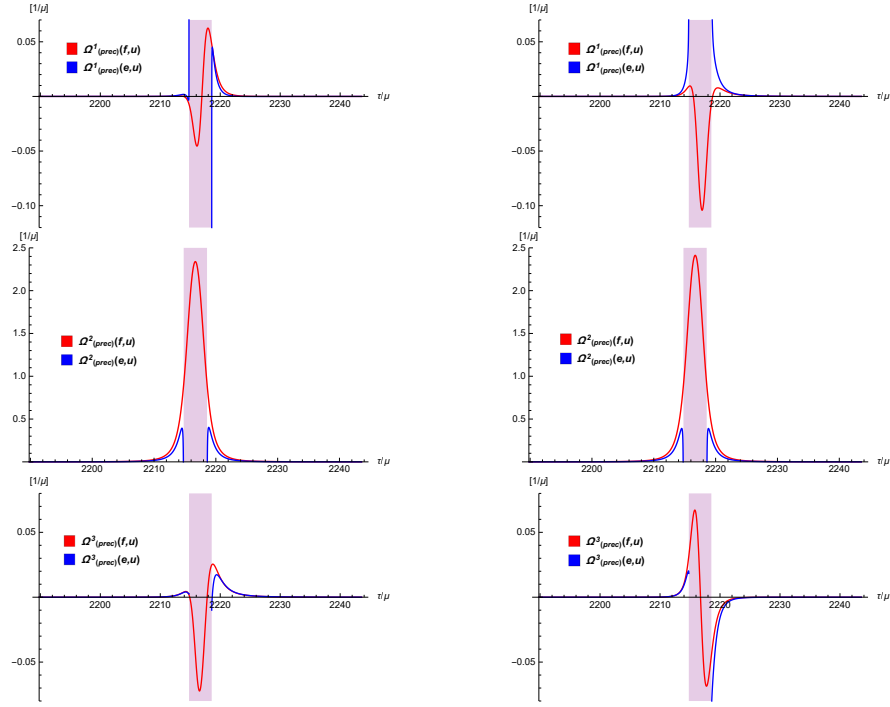


Figure 8: (color online). On the left and right columns the evolutions of the spherical triad components of the spin precessional angular velocities are presented along those orbits which are shown in the left and right columns of Figure 7, respectively.

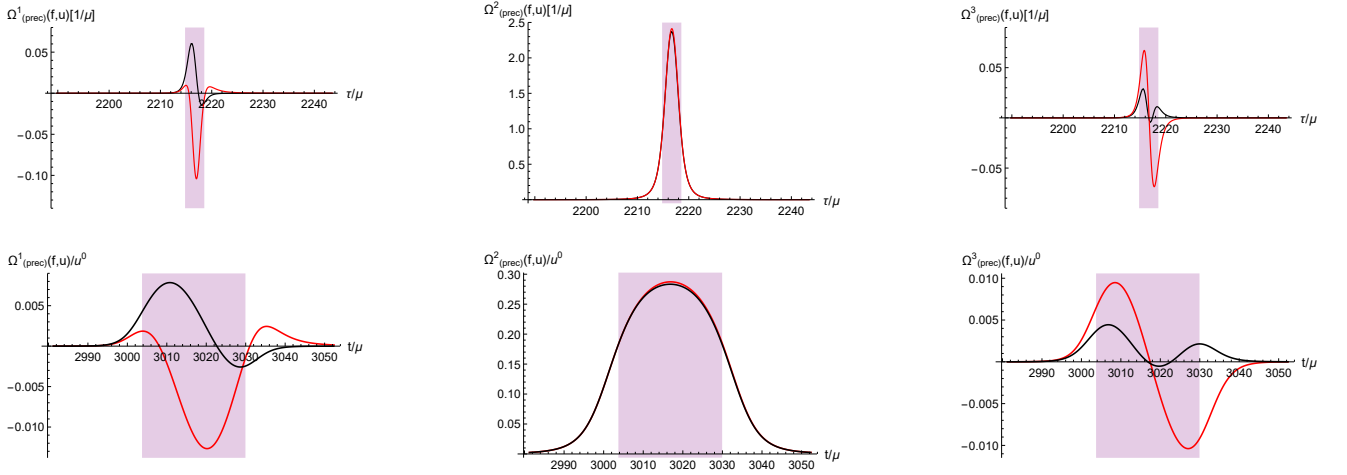


Figure 9: (color online). In the first line, the black and the red curves show the precessional angular velocity spherical frame components without and with spin-curvature coupling, respectively. The second line shows them when the spin evolution is considered as a function of the coordinate time  $t$ . These evolutions belong to the case which is presented in the right hand sides of Figures 7 and 8.

mention that, both functions  $\theta^{(S)}$  and  $\phi^{(S)}$  steeply increase as approaching the edge of the black dots region. Those maxima, which can be seen on the panels, belong to the chosen grid in the  $\hat{E}$ ,  $\hat{J}_z$  plane.

## B. Spinning bodies moving on zoom-whirl orbits in rotating regular black hole spacetimes

In this subsection, we set  $\mu = 0$ ,  $\gamma = 3$  and  $a = 0.99\mu_{em}$ . The background is either a regular, rotating

Bardeen-like ( $\nu = 2$ ) or Hayward-like ( $\nu = 3$ ) black hole spacetime. For  $\nu = 2$  and  $\nu = 3$ , the spacetime contains a black hole for  $q \leq 0.081$  and  $q \leq 0.216$ , respectively.

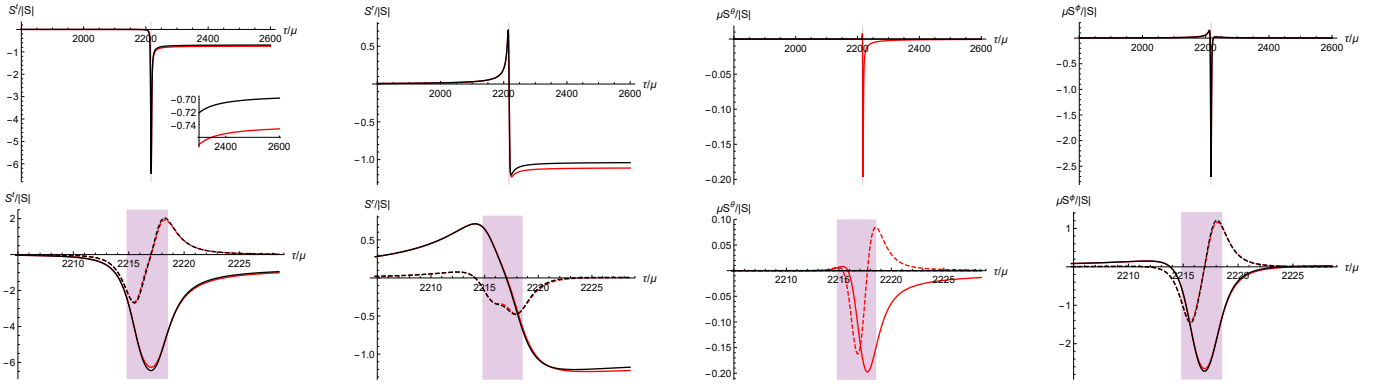


Figure 10: (color online). In the first line, the black and the red curves present the Boyer-Lindquist coordinate components of the unit spin vector without and with spin-curvature coupling. In case of  $S^t$ , the relatively small deviation of the curves when the test body is moving away from the central black hole is shown in a small box. The second line presents the evolutions of the unit spin vector and their derivatives rescaled to dimensionless variables when the spinning test body is close to the central black hole. These evolutions belong to the case, which is presented in the right hand sides of Figures 7 and 8 and also in Figure 9. The time interval, when the body is inside the ergosphere, is indicated by a purplish shadow on all panels.

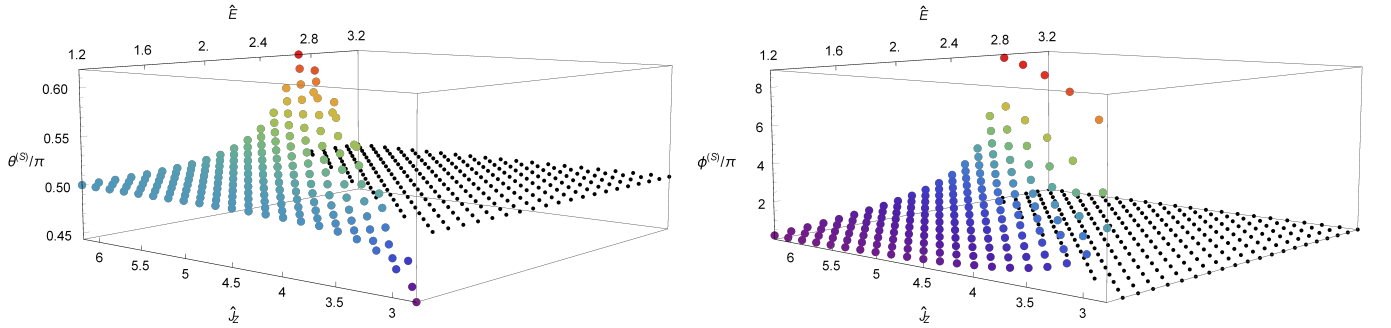


Figure 11: (color online). The left and right panels present the final value of the spin angles  $\theta^{(S)}(\tau^*)$  and  $\phi^{(S)}(\tau^*)$ , respectively, as functions of the dimensionless energy  $\hat{E} = E/M$  and angular momentum  $\hat{J}_z = J_z/\mu M$ . The final values were computed at  $\tau^* = 4433\mu$ . We have checked that the spin angles undergo only insignificant changes for  $\tau > \tau^*$ . The initial spin is given by  $|S|/\mu M = 0.1$ ,  $\theta^{(S)}(0) = \pi/2$  and  $\phi^{(S)}(0) = 0$ . The initial momentum has vanishing  $\theta$  component:  $p^\theta(0)/M = 0$ , and its additional components were determined from  $\hat{E}$ ,  $\hat{J}_z$  and  $p^a p_a/M^2 = -1$ . The small black dots in the plane of the initial spin angles represent the region, where the body crosses the event horizon of the Kerr black hole, hence, unbound orbits do not develop.

We consider three cases:  $(\nu = 2, q = 0.081)$ ,  $(\nu = 3, q = 0.081)$  and  $(\nu = 3, q = 0.216)$ . For these parameters the regular black holes have two stationary limit surfaces and event horizons. In addition, the spin magnitude for the moving body is chosen as  $|S|/\mu M = 0.1$ .

On Figure 12, zoom-whirl orbits in different regular rotating black hole spacetimes are presented. The columns from left to right correspond to  $(\nu = 2, q = 0.081)$ ,  $(\nu = 3, q = 0.081)$  and  $(\nu = 3, q = 0.216)$ . With the notation change  $\mu \rightarrow \mu_{em}$ , the initial values are chosen the same as in the second column of Figure 3. Each row represents the same quantity which was shown on Figure 6. The first two columns show that both the orbit and the spin evolutions are significantly different in the cases of the Bardeen-like and Hayward-like black holes for the same  $\mu_{em}$  and  $q$  values. In addition, the second and the third columns show in the case of Hayward-like background that these evolutions are also sensitive for the value of  $q$ . The way of deviation of the orbit from the equatorial plane, which is the effect of the spin-curvature

coupling, is also very sensitive for the parameters of the regular black holes. The spin vector evolutions including the first whirling period in the boosted SO frame is presented in the third row. The black dots represent a jump in the evolution. The part of the evolution which is not shown takes place inside the ergosphere. The amount of the jumps is somewhat different for each cases. The fourth row shows the total evolution of the spin vector in the boosted ZAMO frame. The final directions (blue arrows) of the spin direction are significantly different. The evolutions of the spherical frame components of the precessional angular velocity including the first three whirling period are shown in the last three rows. These are perturbatively different for the different regular black holes. However, the effects of these small differences add up over the evolution.

Finally, we mention that a consideration of unbound orbits about regular black holes can be found in Ref. [125].

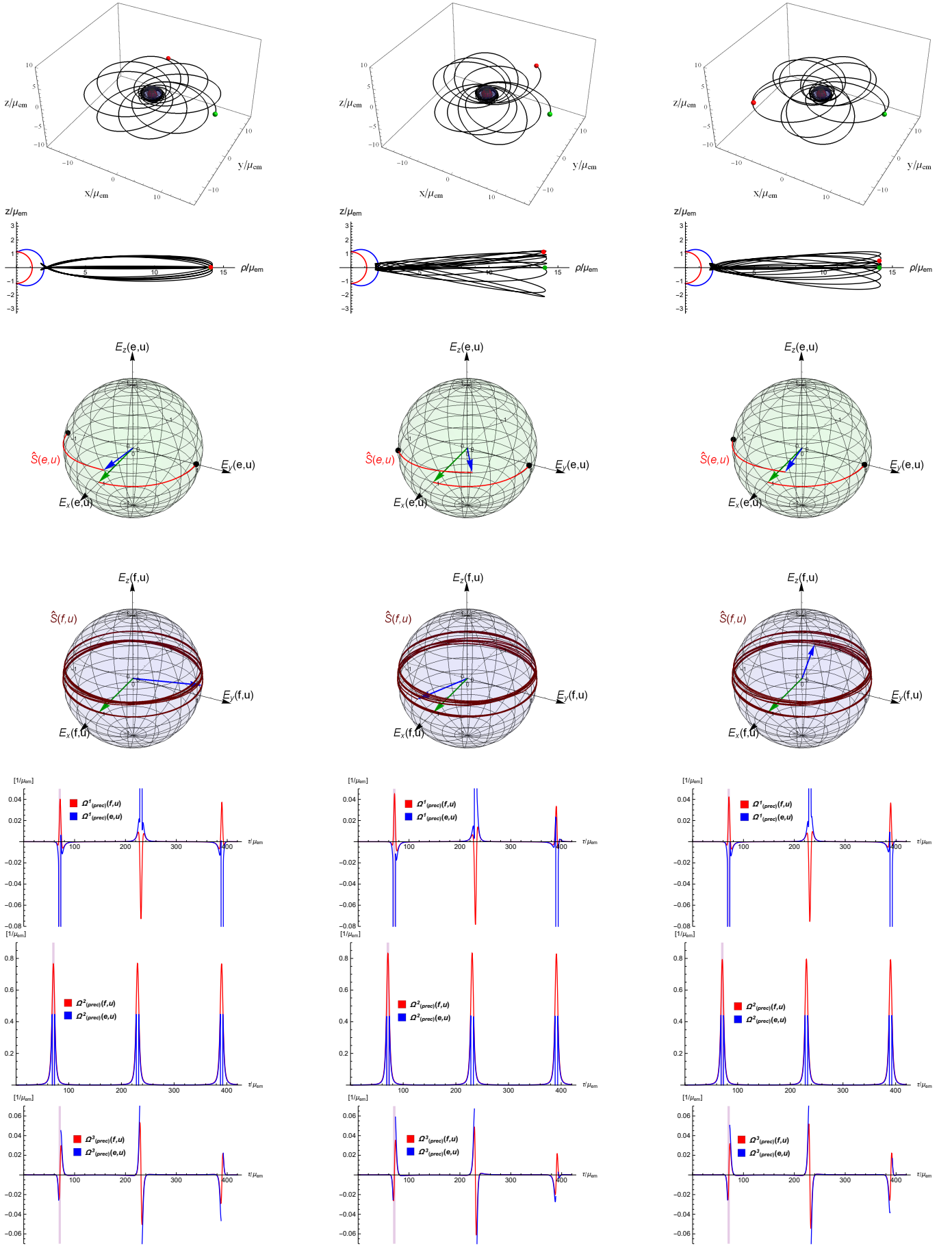


Figure 12: (color online). Zoom-whirl orbits are represented around regular, rotating black holes with  $\gamma = 3$  and  $a = 0.99\mu_{em}$ . The first column shows the orbit around a Bardeen-like black hole ( $\nu = 2$ ) while the middle and the last around a Hayward-like black hole ( $\nu = 3$ ). The parameter  $q$  is 0.081 in the first two columns while 0.216 in third one. Applying the notation change  $\mu \rightarrow \mu_{em}$ , the initial values are chosen the same as in the second column of Figure 3. The quantities in each line are the same which are presented in Figure 6.

## V. CONCLUSIONS

We have considered numerically the evolution of a spinning test body governed by the MPD equations, moving along spherical-like, zoom-whirl and unbound orbits around a Kerr black hole. When the spacetime curvature and the spin contributions on the right hand sides of the MPD equations can be neglected, we recovered the corresponding results of Ref. [92] for a spherical orbit. However, for higher spin, an amplitude modulation occurred in the harmonic evolution of the spin precessional angular velocity caused by the spin-curvature coupling. This amplitude modulation also occurred in the  $\theta$  Boyer-Lindquist coordinate component of the spin vector.

The existence of zoom-whirl orbits are confirmed by using the MPD dynamics. The considered zoom-whirl and unbound orbits of spinning body passed over the ergosphere, where the PN approximation cannot be applied. In all cases the numerical investigations showed that the spin precessional angular velocity highly increased near and inside the ergosphere. Thus the direction of the spin vector is significantly varied during the evolutionary phase inside the ergosphere. The initial values were chosen such that the test body moved in the equatorial plane when the spin-curvature coupling is neglected. Hence, the effect of this coupling occurred as a deviation of the orbit from the equatorial plane. In order to investigate non-trivial spin evolution, the initial spin direction was chosen to be perpendicular to the rotation axis of the central black hole. Then, the spin vector evolved in the equatorial plane of the boosted SO and ZAMO frames when the spin-curvature coupling is neglected. The deviation of the spin vector from this equatorial plane was also the effect of the spin-curvature coupling. Additional effects of the spin-curvature coupling was observed in the evolutions of the spin precessional angular velocity and of the Boyer-Lindquist coordinate components of the spin vector.

Zoom-whirl orbits and spin precession including the spin-curvature coupling were also considered in regular spacetimes containing a central rotating black hole. Significant differences were observed in the way of deviation of the orbit from the equatorial plane which were sensitive for the parameters of the regular black hole. Small deviations were found in the spin precession angular velocity, which add up over the evolutions. Hence, the direction of the final spin vector can be very different for different parameters of the regular black hole.

Finally, we mention that the numeric investigation presented here could be generalized in the following way. Besides the spin-curvature coupling another effects would occur if the backreaction of the body to the metric was not neglected. This backreaction appears as a self-force in the equation of motion [126–129], and also causes a deviation from the geodesic orbit like the spin-curvature coupling.

## Acknowledgements

The work of B. M. was supported by the János Bolyai Research Scholarship of the Hungarian Academy of Sciences. The work of Z. K. was supported by the János Bolyai Research Scholarship of the Hungarian Academy of Sciences, by the UNKP-18-4 New National Excellence Program of the Ministry of Human Capacities and by the Hungarian National Research Development and Innovation Office (NKFI) in the form of the grant 123996.

## VI. CONFLICT OF INTEREST

The authors declare no conflict of interest.

## VII. APPENDIX A: THE RELATION BETWEEN THE FRAMES $E_\alpha(e, U)$ AND $E_\alpha(f, U)$

The frame vectors  $E_\alpha(e, U)$  derived from the SO's frame are the following linear combination of  $E_\alpha(f, U)$ :

$$\begin{aligned} E_1(e, U) &= E_1(f, U) + \frac{\Gamma_{(Z)} w_{(Z)}^1}{1 + \Gamma_{(S)}} \left[ \frac{a\mathcal{B} \sin \theta}{\sqrt{-g_{tt}\Sigma\mathcal{A}}} E_3(f, U) + \left( 1 - \sqrt{\frac{\Sigma\Delta}{-g_{tt}\mathcal{A}}} \right) \frac{\Gamma_{(Z)} \mathbf{w}_{(Z)}}{1 + \Gamma_{(Z)}} \right], \\ E_2(e, U) &= E_2(f, U) + \frac{\Gamma_{(Z)} w_{(Z)}^2}{1 + \Gamma_{(S)}} \left[ \frac{a\mathcal{B} \sin \theta}{\sqrt{-g_{tt}\Sigma\mathcal{A}}} E_3(f, U) + \left( 1 - \sqrt{\frac{\Sigma\Delta}{-g_{tt}\mathcal{A}}} \right) \frac{\Gamma_{(Z)} \mathbf{w}_{(Z)}}{1 + \Gamma_{(Z)}} \right], \\ E_3(e, U) &= \left( \sqrt{\frac{\Sigma\Delta}{-g_{tt}\mathcal{A}}} + \Gamma_{(Z)} \right) \frac{E_3(f, U)}{1 + \Gamma_{(S)}} - \frac{\Gamma_{(Z)} \mathbf{w}_{(Z)}}{1 + \Gamma_{(S)}} \left[ \left( 1 - \sqrt{\frac{\Sigma\Delta}{-g_{tt}\mathcal{A}}} \right) \frac{\Gamma_{(Z)} w_{(Z)}^3}{1 + \Gamma_{(Z)}} + \frac{a\mathcal{B} \sin \theta}{\sqrt{-g_{tt}\Sigma\mathcal{A}}} \right]. \end{aligned} \quad (64)$$

The inverse relations are

$$E_1(f, U) = E_1(e, U) - \frac{\Gamma_{(S)} w_{(S)}^1}{1 + \Gamma_{(Z)}} \left[ \frac{a\mathcal{B} \sin \theta}{\sqrt{-g_{tt}\Sigma\mathcal{A}}} E_3(e, U) - \left( 1 - \sqrt{\frac{\Sigma\Delta}{-g_{tt}\mathcal{A}}} \right) \frac{\Gamma_{(S)} \mathbf{w}_{(S)}}{1 + \Gamma_{(S)}} \right],$$

$$E_2(f, U) = E_2(e, U) - \frac{\Gamma_{(S)} w_{(S)}^2}{1 + \Gamma_{(Z)}} \left[ \frac{a\mathcal{B} \sin \theta}{\sqrt{-g_{tt}\Sigma\mathcal{A}}} E_3(e, U) - \left( 1 - \sqrt{\frac{\Sigma\Delta}{-g_{tt}\mathcal{A}}} \right) \frac{\Gamma_{(S)} \mathbf{w}_{(S)}}{1 + \Gamma_{(S)}} \right],$$

$$E_3(f, U) = \left( \sqrt{\frac{\Sigma\Delta}{-g_{tt}\mathcal{A}}} + \Gamma_{(S)} \right) \frac{E_3(e, U)}{1 + \Gamma_{(Z)}} - \frac{\Gamma_{(S)} \mathbf{w}_{(S)}}{1 + \Gamma_{(Z)}} \left[ \left( 1 - \sqrt{\frac{\Sigma\Delta}{-g_{tt}\mathcal{A}}} \right) \frac{\Gamma_{(S)} w_{(S)}^3}{1 + \Gamma_{(S)}} - \frac{a\mathcal{B} \sin \theta}{\sqrt{-g_{tt}\Sigma\mathcal{A}}} \right]. \quad (65)$$

The frame components of any vector field

$$\mathbf{V} = V^\alpha{}^{(e)} E_\alpha(e) = V^\alpha{}^{(f)} E_\alpha(f), \quad (66)$$

obey the following transformation rule

$$V^1{}^{(e)} = V^1{}^{(f)} + \left[ \left( 1 - \sqrt{\frac{\Sigma\Delta}{-g_{tt}\mathcal{A}}} \right) \frac{\Gamma_{(Z)} \mathbf{w}_{(Z)} \cdot \mathbf{V}}{1 + \Gamma_{(Z)}} + \frac{a\mathcal{B} \sin \theta}{\sqrt{-g_{tt}\Sigma\mathcal{A}}} V^3{}^{(f)} \right] \frac{\Gamma_{(Z)} w_{(Z)}^1}{1 + \Gamma_{(S)}},$$

$$V^2{}^{(e)} = V^2{}^{(f)} + \left[ \left( 1 - \sqrt{\frac{\Sigma\Delta}{-g_{tt}\mathcal{A}}} \right) \frac{\Gamma_{(Z)} \mathbf{w}_{(Z)} \cdot \mathbf{V}}{1 + \Gamma_{(Z)}} + \frac{a\mathcal{B} \sin \theta}{\sqrt{-g_{tt}\Sigma\mathcal{A}}} V^3{}^{(f)} \right] \frac{\Gamma_{(Z)} w_{(Z)}^2}{1 + \Gamma_{(S)}},$$

$$V^3{}^{(e)} = \left( \sqrt{\frac{\Sigma\Delta}{-g_{tt}\mathcal{A}}} + \Gamma_{(Z)} \right) \frac{V^3{}^{(f)}}{1 + \Gamma_{(S)}} - \frac{\Gamma_{(Z)} \mathbf{w}_{(Z)} \cdot \mathbf{V}}{1 + \Gamma_{(S)}} \left[ \frac{a\mathcal{B} \sin \theta}{\sqrt{-g_{tt}\Sigma\mathcal{A}}} + \left( 1 - \sqrt{\frac{\Sigma\Delta}{-g_{tt}\mathcal{A}}} \right) \frac{\Gamma_{(Z)} w_{(Z)}^3}{1 + \Gamma_{(Z)}} \right], \quad (67)$$

with  $\mathbf{w}_{(Z)}$  introduced in Equation (27).

The inverse relations are

$$V^1{}^{(f)} = V^1{}^{(e)} + \left[ \left( 1 - \sqrt{\frac{\Sigma\Delta}{-g_{tt}\mathcal{A}}} \right) \frac{\Gamma_{(S)} \mathbf{w}_{(S)} \cdot \mathbf{V}}{1 + \Gamma_{(S)}} - \frac{a\mathcal{B} \sin \theta}{\sqrt{-g_{tt}\Sigma\mathcal{A}}} V^3{}^{(e)} \right] \frac{\Gamma_{(S)} w_{(S)}^1}{1 + \Gamma_{(Z)}},$$

$$V^2{}^{(f)} = V^2{}^{(e)} + \left[ \left( 1 - \sqrt{\frac{\Sigma\Delta}{-g_{tt}\mathcal{A}}} \right) \frac{\Gamma_{(S)} \mathbf{w}_{(S)} \cdot \mathbf{V}}{1 + \Gamma_{(S)}} - \frac{a\mathcal{B} \sin \theta}{\sqrt{-g_{tt}\Sigma\mathcal{A}}} V^3{}^{(e)} \right] \frac{\Gamma_{(S)} w_{(S)}^2}{1 + \Gamma_{(Z)}},$$

$$V^3{}^{(f)} = \left( \sqrt{\frac{\Sigma\Delta}{-g_{tt}\mathcal{A}}} + \Gamma_{(S)} \right) \frac{V^3{}^{(e)}}{1 + \Gamma_{(Z)}} + \frac{\Gamma_{(S)} \mathbf{w}_{(S)} \cdot \mathbf{V}}{1 + \Gamma_{(Z)}} \left[ \frac{a\mathcal{B} \sin \theta}{\sqrt{-g_{tt}\Sigma\mathcal{A}}} - \left( 1 - \sqrt{\frac{\Sigma\Delta}{-g_{tt}\mathcal{A}}} \right) \frac{\Gamma_{(S)} w_{(S)}^3}{1 + \Gamma_{(S)}} \right], \quad (68)$$

with  $\mathbf{w}_{(S)}$  introduced in Equation (24).

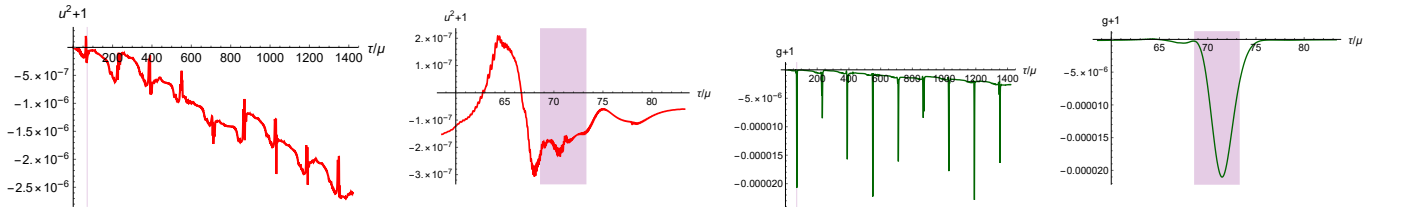


Figure 13: (color online). The evolutions of  $u^2 = u_a u^a$  and  $g$  on longer and shorter timescales for a zoom-whirl orbit presented on the left hand sides of Figures 3 and 4.

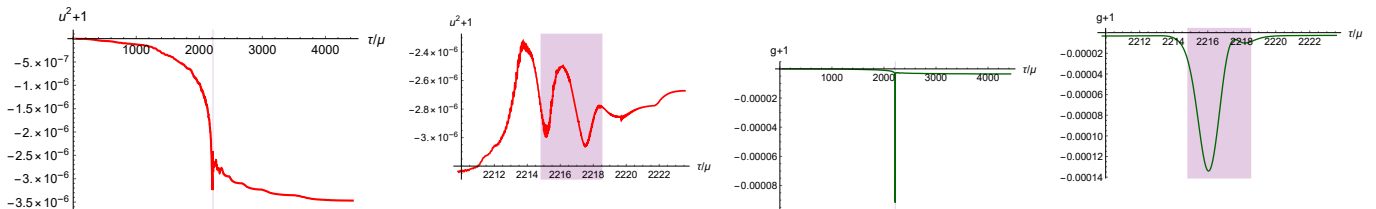


Figure 14: (color online). The evolutions of  $u^2 = u_a u^a$  and  $g$  on longer and shorter timescales are shown for an unbound orbit presented on the left hand sides of Figures 7 and 8.

## VIII. APPENDIX B: CHECKING THE VALIDITY OF THE MPD EQUATIONS

The contraction of the inverse of the velocity-momentum relation (6) with  $u_a$  gives that the sign of  $p_a u^a$  is determined by the quantity:

$$g = u_a u^a - \frac{1}{2M^2} u^b R_{ebcd} S^{cd} S^{ae} u_a, \quad (69)$$

which corresponds to  $\dot{x}\tilde{T}\dot{x} = \dot{x}G\dot{x}$  in Ref. [119]. Both the functions  $g$  and  $u_a u^a$  are shown on Figures 13 and 14 for two cases when the test body follows a zoom-whirl and an unbound orbit, respectively. In both cases  $g$  takes values close to -1 during the whole evolution and  $u_a u^a = -1$ . Hence, the MPD equations are applied where they are valid. Similar is hold along the all trajectories presented in the article.

- 
- [1] LIGO Scientific Collaboration and Virgo Collaboration, *Phys. Rev. Lett.* **2016**, *116*, 061102.
  - [2] LIGO Scientific Collaboration and Virgo Collaboration, *Phys. Rev. Lett.* **2016**, *116*, 241103.
  - [3] LIGO Scientific Collaboration and Virgo Collaboration, *Phys. Rev. Lett.* **2017**, *118*, 221101.
  - [4] LIGO Scientific Collaboration and Virgo Collaboratio, *Phys. Rev. Lett.* **2017**, *119*, 141101.
  - [5] LIGO Scientific Collaboration and Virgo Collaboratio, *Phys. Rev. Lett.* **2017**, *119*, 161101.
  - [6] LIGO Scientific Collaboration and Virgo Collaboration, *Astrophys. J. Lett.* **2017**, *848*, L13.
  - [7] LIGO Scientific Collaboration and Virgo Collaboration, *Astrophys. J.* **2017**, *851*, L35.
  - [8] LIGO Scientific Collaboration and Virgo Collaboration, *Phys. Rev. X* **2019**, *9*, 031040.
  - [9] C. Kimball, C. P. L. Berry, V. Kalogera, *Res. Notes AAS* **2020**, *4*, 2.
  - [10] E. Kun, K. É. Gabányi, M. Karouzos, S. Britzen, L. Á. Gergely, *Mon. Not. Royal Astron. Soc.* **2014**, *445* (2), 1370.
  - [11] B. M. Barker, R. F. O'Connell, *Phys. Rev. D* **1970**, *2*, 1428.
  - [12] B. M. Barker, R. F. O'Connell, *Phys. Rev. D* **1975**, *12*, 329.
  - [13] L. E. Kidder, *Phys. Rev. D* **1995**, *52*, 821.
  - [14] E. Poisson, *Phys. Rev. D* **1998**, *57*, 5287.
  - [15] N. Wex, *Class. Quantum Grav.* **1995** *12*, 983.
  - [16] C. Königsdörffer, A. Gopakumar, *Phys. Rev. D* **2005**, *71*, 024039.
  - [17] Z. Keresztes, B. Mikóczi, L. Á. Gergely, *Phys. Rev. D* **2005**, *71*, 124043.
  - [18] C. Königsdörffer, A. Gopakumar, *Phys. Rev. D* **2006**, *73*, 044011.
  - [19] É. Racine, *Phys. Rev. D* **2008**, *78*, 044021.
  - [20] M. Kesden, D. Gerosa, R. O'Shaughnessy, E. Berti, U. Sperhake, *Phys. Rev. Lett.* **2015**, *114*, 081103.
  - [21] T. A. Apostolatos, C. Cutler, G. J. Sussman, K. S. Thorne, *Phys. Rev. D* **1994**, *49*, 6274.
  - [22] J. D. Schnittman, *Phys. Rev. D* **2004**, *70*, 124020 (2004).
  - [23] L. Á. Gergely, P. L. Biermann, *Astrophys. J.* **2009** *697*, 1621.
  - [24] C. O. Lousto, J. Healy, *Phys. Rev. Lett.* **2015**, *114*, 141101. [arXiv:1410.3830]
  - [25] D. Gerosa, A. Lima, E. Berti, U. Sperhake, M. Kesden, R. O'Shaughnessy, *Class. Quantum Grav.* **2019** *36*, 10, 105003.
  - [26] M. Mathisson, *Acta. Phys. Polon.* **1937**, *6*, 163.
  - [27] A. Papapetrou, *Proc. Phys. Soc.* **1951** *64*, 57.
  - [28] W. Dixon, *Nuovo Cim.* **1964** *34*, 317.
  - [29] W. G. Dixon, *Proc. R. Soc. London A* **1970**, *314*, 499.
  - [30] W. G. Dixon, in *Isolated Gravitating Systems in General Relativity*, Proceedings of the International School of Physics, Course LXVII **1979**, ed. by J. Ehlers.
  - [31] P. Amaro-Seoane et al., *Laser Interferometer Space Antenna* **2017**, arXiv:1702.00786.
  - [32] C. Huwylar, E. K. Porter, P. Jetzer, *Phys. Rev. D* **2015**, *91*, 024037.
  - [33] J. N. Bahcall, R. A. Wolf, *Astrophys. J.* **1977** *216*, 883.
  - [34] I. Bartos, Z. Haiman, B. Kocsis, Sz. Márka, *Phys. Rev. Lett.* **2013**, *110*, 221102.
  - [35] C. J. Hailey, K. Mori, F. E. Bauer, M. E. Berkowitz, J. Hong, B. J. Hord, *Nature* **2018**, *556*, 70.
  - [36] B. Mikóczi, *Phys. Rev. D* **2017**, *95*, 064023.
  - [37] J. Frenkel, *Z. Phys.* **1926** *37*, 243.
  - [38] F. A. E. Pirani, *Acta Phys. Polon.* **1956**, *15*, 389.
  - [39] E. Corinaldesi, A. Papapetrou, *Proc. Roy. Soc. A* **1951**, *209*, 259.
  - [40] T. D. Newton, E. P. Wigner, *Rev. Mod. Phys.* **1949**, *21*, 400.
  - [41] M. H. L. Pryce, *Proc. Roy. Soc. Lond. A* **1948**, *195*, 62.

- [42] W. M. Tulczyjew, *Acta Phys. Polon.* **1959**, *18*, 393.
- [43] A. Ohashi, *Phys. Rev. D* **2003**, *68*, 044009.
- [44] K. Kyrian, O. Semerák, *Mon. Not. Roy. Astron. Soc.* **2007**, *382*, 1922.
- [45] V. Witzany, J. Steinhoff, G. Lukes-Gerakopoulos, *Class. Quantum Grav.* **2019**, *36*, 075003.
- [46] E. Barausse, E. Racine, A. Buonanno, *Phys. Rev. D* **2009**, *80*, 104025; Erratum: *Phys. Rev. D* **2012** *85*, 069904(E).
- [47] A. A. Deriglazov, W. G. Ramirez, *Phys. Rev. D* **2015**, *92*, 124017.
- [48] G. Lukes-Gerakopoulos, J. Seyrich, D. Kunst, *Phys. Rev. D* **2014**, *90*, 1040109.
- [49] D. Kunst, T. Ledvinka, G. Lukes-Gerakopoulos, J. Seyrich, *Phys. Rev. D* **2016**, *93*, 044004.
- [50] B. M. Barker, R. F. O'Connell, *Gen. Rel. Grav.* **1974**, *5*, 539.
- [51] O. Semerák, *Mon. Not. Roy. Astron. Soc.* **1999**, *308*, 863.
- [52] S. Suzuki, K. Maeda, *Phys. Rev. D* **1998**, *58*, 023005.
- [53] M. D. Hartl, *Phys. Rev. D* **2003**, *67*, 104023.
- [54] M. D. Hartl, *Phys. Rev. D* **2003**, *67*, 024005.
- [55] W.-B. Han, *Gen. Relativ. Gravit.* **2008**, *40*, 1831.
- [56] W.-B. Han, R. Cheng, *Gen. Relativ. Gravit.* **2017**, *49*, 48.
- [57] B. Mashhoon, D. Singh, *Phys. Rev. D* **2006**, *74*, 124006.
- [58] D. Bini, P. Fortini, A. Geralico, A. Ortolan, *Class. Quantum Grav.* **2008**, *25*, 125007.
- [59] D. Bini, A. Geralico, *Phys. Rev. D* **2011**, *84*, 104012.
- [60] R. Plyatsko, M. Fenyk, *Phys. Rev. D* **2013**, *87*, 044019.
- [61] D. Bini, A. Geralico, *Class. Quantum Grav.* **2014**, *31*, 075024.
- [62] D. Bini, G. Faye, A. Geralico, *Phys. Rev. D* **2015** *92*, 104003.
- [63] E. Hackmann, C. Lämmerzahl, Y. N. Obukhov, D. Puetzfeld, I. Schaffer, *Phys. Rev. D* **2014**, *90*, 064035.
- [64] G. Lukes-Gerakopoulos, *Phys. Rev. D* **2017**, *96*, 104023.
- [65] U. Ruangsri, S. J. Vigeland, S. A. Hughes, *Phys. Rev. D* **2016**, *94*, 044008.
- [66] B. Toshmatov, D. Malafarina, *Phys. Rev. D* **2019**, *100*, 104052.
- [67] B. Toshmatov, O. Rahimov, B. Ahmedov, D. Malafarina, *Eur. Phys. J. C* **2020**, *80*, 675.
- [68] C. A. Benavides-Gallego, W.-B. Han, D. Malafarina, *Phys. Rev. D* **2021**, *104*, 084024.
- [69] K. Glampedakis, D. Kennefick, *Phys. Rev. D* **2002**, *66*, 044002.
- [70] K. Glampedakis, S. A. Hughes, D. Kennefick, *Phys. Rev. D* **2002**, *66*, 064005.
- [71] K. Glampedakis, *Class. Quantum Grav.* **2005**, *22*, S605.
- [72] J. Levin, G. Perez-Giz, *Phys. Rev. D* **2008**, *77*, 103005.
- [73] R. Grossman, J. Levin, G. Perez-Giz, *Phys. Rev. D* **2012**, *85*, 023012.
- [74] F. Pretorius, D. Khurana, *Class. Quantum Grav.* **2007**, *24*, S83.
- [75] J. Healy, J. Levin, D. Shoemaker, *Phys. Rev. Lett.* **2009**, *103*, 131101.
- [76] U. Sperhake, V. Cardoso, F. Pretorius, E. Berti, T. Hinderer, N. Yunes *Phys. Rev. Lett.* **2009**, *103*, 131102.
- [77] R. Gold, B. Bruggmann, *Class. Quantum Grav.* **2010**, *27*, 084035.
- [78] R. Gold, B. Bruggmann, *Phys. Rev. D* **2013**, *88*, 064051.
- [79] W. E. East, S. T. McWilliams, J. Levin, F. Pretorius, *Phys. Rev. D* **2013**, *87*, 043004.
- [80] J. Levin, R. Grossman, *Phys. Rev. D* **2009**, *79*, 043016.
- [81] R. Grossman, J. Levin, *Phys. Rev. D* **2009**, *79*, 043017.
- [82] L. De Vittori, A. Gopakumar, A. Gupta, P. Jetzer, *Phys. Rev. D* **2014**, *90*, 124066.
- [83] D. Bini, A. Geralico, J. Vines, *Phys. Rev. D* **2017**, *96*, 084044.
- [84] J. M. Bardeen, *Proc. GR5, Tbilisi USSR* **1968**, 174.
- [85] E. Ayón-Beato, A. García, *Phys. Lett. B* **2000**, *493*, 149.
- [86] S. A. Hayward, *Phys. Rev. Lett.* **2006**, *96*, 031103.
- [87] Z.-Y. Fan, X. Wang, *Phys. Rev. D* **2016**, *94*, 124027.
- [88] B. Toshmatov, Z. Stuchlík, B. Ahmedov, *Phys. Rev. D* **2017**, *95*, 084037.
- [89] K. A. Bronnikov, *Phys. Rev. D* **2017**, *96*, 128501.
- [90] M. E. Rodrigues, E. L. B. Junior, *Phys. Rev. D* **2017**, *96*, 128502.
- [91] B. Toshmatov, Z. Stuchlík, B. Ahmedov, *Note on the character of the generic rotating charged regular black holes in general relativity coupled to nonlinear electrodynamics*, **2017** [arXiv:1712.04763].
- [92] D. Bini, A. Geralico, R. T. Jantzen, *Phys. Rev. D* **2017**, *95*, 124022.
- [93] E. Hackmann, C. Lämmerzahl, Y. N. Obukhov, D. Puetzfeld, I. Schaffer *Phys. Rev. D* **2014**, *90*, 064035.
- [94] D. Bini, A. Geralico, *Phys. Rev. D* **2018**, *98*, 084021.
- [95] K. P. Tod, F. de Felice, M. Calvani, *Il Nuovo Cimento* **1976**, *34*, 365.
- [96] R. Hojman, S. Hojman, *Phys. Rev. D* **1977**, *15*, 2724.
- [97] L. F. O. Costa, G. Lukes-Gerakopoulos, O. Semerák, *Phys. Rev. D* **2018**, *97*, 084023.
- [98] S. Suzuki, K. Maeda, *Phys. Rev. D* **1997**, *55*, 4848.
- [99] R. P. Kerr, *Phys. Rev. Lett.* **1963**, *11*, 237.
- [100] J. M. Bardeen, P. W. H. Teukolsky, *Astrophys. J.* **1972**, *178*, 347.
- [101] O. Semerák, *Gen. Rel. Grav.* **1993**, *25*, 1041.
- [102] E. P. Wigner, *Annals. Math.* **1939**, *40*, 149 [*Nucl. Phys. Proc. Suppl.* **1989**, *6*, 9].
- [103] D. Bini, A. Geralico, R. T. Jantzen, *Phys. Rev. D* **2019**, *99*, 064041.
- [104] C. W. Misner, K. S. Thorne, J. A. Wheeler, *Gravitation*, W. H. Freeman and Company, San Francisco **1973**.
- [105] J. L. Synge, *Relativity of the general theory*, North-Holland Publishing Company, Amsterdam **1960**.
- [106] H. S. Ruse, *Quart. J. Math.* **1930** *1*, 146.
- [107] P. Gunther, *Arch. Rat. Mech. Anal.* **1965**, *18*, 103.
- [108] H. A. Buchdahl, *Gen. Rel. Grav.* **1972**, *3*, 35.
- [109] H. A. Buchdahl, N. P. Warner, *J. Phys. A* **1980** *13*, 509.
- [110] R. W. John, *Ann. Phys. Leipzig* **1984**, *41*, 67.
- [111] R. W. John, *Trans. Inst. Phys. Estonian Acad. Sci.* **1989**, *65*, 58.
- [112] M. D. Roberts, *Astrophys. Lett. Comm.* **1993**, *28*, 349.
- [113] J. Steinhoff, *Spin gauge symmetry in the action principle for classical relativistic particles*, **2015** [arXiv:1501.04951].
- [114] L. F. O. Costa, C. Herdeiro, J. Natário, M. Zilhão, *Phys. Rev. D* **2012**, *85*, 024001.
- [115] L. F. O. Costa, J. Natário, *Fund. Theor. Phys.* **2015**, *179*, 215.
- [116] L. F. O. Costa, J. Natário, M. Zilhão, *Phys. Rev. D* **2016**, *93*, 104006.
- [117] I. Timogiannis, G. Lukes-Gerakopoulos, T. A. Apostolatos, *Phys. Rev. D* **2021**, *104*, 024042.
- [118] A. A. Deriglazov, W. G. Ramirez, *Int. J. Mod. Phys. D* **2017**, *26*, 1750047.

- [119] A. A. Deriglazov, W. G. Ramirez, *Adv. Math. Phys.* **2017**, 7397159.
- [120] A. A. Deriglazov, W. G. Ramirez, *Phys. Lett. B* **2018**, 779, 210.
- [121] A. J. Hanson, T. Regge, *Ann. Phys.* **1974**, 87, 498.
- [122] J. Ehlers, E. Rudolph, *Gen. Relativ. Gravit.* **1977**, 8, 197.
- [123] T. Tanaka, Y. Mino, M. Sasaki, M. Shibata, *Phys. Rev. D* **1996**, 54, 3762.
- [124] S. A. Hojman, F. A. Asenjo, *Class. Quantum. Grav.* **2012**, 30, 025008.
- [125] Z. Keresztes, B. Mikóczy, *Roman. Astron. J.* **2020**, 30, 59.
- [126] A. Pound, *Phys. Rev. Lett.* **2012**, 109, 051101.
- [127] M. van de Meent, *Phys. Rev. D* **2018**, 97, 104033.
- [128] L. Barack, A. Pound, *Rep. Prog. Phys.* **2018**, 82, 016904.
- [129] L. Barack, M. Colleoni, T. Damour, S. Isoyama, N. Sago, *Phys. Rev. D* **2019**, 100, 124015.